

CHEMOUT: CHEMical complexity in star-forming regions of the OUTER Galaxy

IV. ALMA observations of organic species at Galactocentric radius ~ 23 kpc

F. Fontani^{1,2,3}, G. Vermariën⁴, S. Viti⁴, D. Gigli^{1,5}, L. Colzi⁶, M.T. Beltrán¹, P. Caselli², V.M. Rivilla⁶, and A. Sánchez-Monge^{7,8}

¹ INAF - Osservatorio Astrofisico di Arcetri, Largo E. Fermi 5, I-50125, Florence, Italy
e-mail: francesco.fontani@inaf.it

² Max-Planck-Institut für extraterrestrische Physik, Giessenbachstraße 1, 85748 Garching bei München, Germany

³ LERMA, Observatoire de Paris, PSL Research University, CNRS, Sorbonne Université, F-92190 Meudon, France

⁴ Leiden Observatory, Leiden University, PO Box 9513, 2300 RA Leiden, The Netherlands

⁵ Leiden Observatory, Leiden University, PO Box 9513, 2300 RA Leiden, The Netherlands

⁶ Dipartimento di Fisica e Astronomia, Università di Firenze, Via G. Sansone 1, 50019 Sesto Fiorentino, Firenze, Italy

⁷ Centro de Astrobiología (CSIC-INTA), Ctra Ajalvir km 4, 28850, Torrejón de Ardoz, Madrid, Spain

⁸ Institut de Ciències de l'Espai (ICE, CSIC), Campus UAB, Carrer de Can Magrans s/n, 08193, Bellaterra (Barcelona), Spain

⁹ Institut d'Estudis Espacials de Catalunya (IEEC), 08860 Castelldefels (Barcelona), Spain

Received XXX; accepted XXX

ABSTRACT

Context. Single-dish observations suggest that the abundances of organic species in star-forming regions of the outer Galaxy, characterised by sub-Solar metallicities, are comparable to those found in the local Galaxy.

Aims. To understand this counter-intuitive result, and avoid misleading interpretation due to beam dilution effects at such large distances, spatially resolved molecular emission maps are needed to link correctly measured abundances and local physical properties.

Methods. We observed several organic molecules with the Atacama Large Millimeter Array towards WB89-671, the source with the largest Galactocentric distance (23.4 kpc) of the project "CHEMical complexity in star-forming regions of the OUTER Galaxy" (CHEMOUT), at a resolution of ~ 15000 au. We compared the observed molecular abundances with chemical model predictions.

Results. We detected emission of c -C₃H₂, C₄H, CH₃OH, H₂CO, HCO, H¹³CO⁺, HCS⁺, CS, HN¹³C, and SO. The emission morphology is complex, extended, and different in each tracer. In particular, the most intense emission in H¹³CO⁺, H₂CO and c -C₃H₂ arises from two millimeter continuum, infrared-bright cores. The most intense CH₃OH and SO emission arises predominantly from the part of the filament with no continuum sources. The narrow linewidths across the filament indicate quiescent gas, despite the two embedded protostars. Derived molecular column densities are comparable with those in local star-forming regions, and suggest anti-correlation between hydrocarbons, ions, HCO, and H₂CO on one side, and CH₃OH and SO on the other.

Conclusions. Static chemical models that best match the observed column densities favour low energetic conditions, expected at large Galactocentric radii, but carbon elemental abundances 3 times higher than that derived extrapolating the [C/H] Galactocentric gradient at 23 kpc. This would indicate a flatter [C/H] trend at large Galactocentric radii, in line with a flat abundance of organics. However, to properly reproduce the chemical composition of each region, models should include dynamical evolution.

Key words. astrochemistry – line: identification – ISM: molecules – stars: formation

1. Introduction

The outer Galaxy (OG), i.e. the part of the Milky Way that extends out of the Solar circle to the outermost edge of the Galactic disc (~ 27 kpc, López-Corredoira et al. 2018), was believed to be an environment not optimal for the formation of molecules and planetesimals. The reason is its sub-Solar metallicity, i.e. the low abundance of elements heavier than helium. In particular, the elemental abundances of oxygen, carbon, and nitrogen, i.e. the three most abundant elements in the Universe after hydrogen and helium, and the most important biogenic elements, decrease as a function of the Galactocentric distance, R_{GC} (Esteban et al. 2017; Arellano-Córdova et al. 2020; Méndez-Delgado et al. 2022). For example, the fractional abundance of oxygen relative to hydrogen, [O/H], decreases gradually from the inner Galaxy to the OG, reaching $\sim 1/5$ th of the Solar value at about 20

kpc (see e.g. Esteban et al. 2017; Méndez-Delgado et al. 2022). For carbon, the decrease of the [C/H] ratio is even more pronounced, reaching $\sim 1/7$ th– $1/8$ th of the Solar value at ~ 20 kpc (Arellano-Córdova et al. 2020; Méndez-Delgado et al. 2022). Such low abundances of heavy elements in the OG suggested in the past that this zone was not suitable for forming planetary systems in which Earth-like planets could be born and might be capable of sustaining life (Ramírez et al. 2010). For this reason, the OG was excluded from the so-called Galactic Habitable Zone (GHZ), which is the portion of the Milky Way with the highest chance to form and develop complex forms of life on (exo-)planets (Gonzalez et al. 2001). Because of this, its chemical complexity has been so far little explored.

However, we are discovering that the presence of small, terrestrial planets is independent on the Galactocentric distance

(e.g. Buchhave et al. 2012; Maliuk & Budaj 2020), and that molecules, including complex organic molecules (COMs, organic species with 6 or more atoms), are found to be more-than-expected abundant in star-forming regions with metallicity lower than Solar, both in the OG (e.g. Blair et al. 2008; Shimonishi et al. 2021; Bernal et al. 2021; Fontani et al. 2022a) and in external galaxies (e.g. Shimonishi et al. 2018; Sewilo et al. 2018). However, molecular formation processes could be different from those in the inner or local Galaxy due to the difference in both metallicity and other environmental conditions. For example, UV irradiation from high-mass stars should be lower, on average, in the OG due to the smaller concentration of high-mass stars. Therefore, abundances of species sensitive to this parameter could be affected also by this environmental change. It is thus crucial to observe molecules in star-forming regions of the OG to constrain models adapted to such sub-Solar metallicity environments.

The few studies performed so far in the OG mentioned above have provided abundances only of a limited number of abundant species, and hence they can answer only partial questions. Blair et al. (2008), Bernal et al. (2021), and Fontani et al. (2022b) detected formaldehyde (H_2CO) and methanol (CH_3OH) in star-forming regions of the OG up to 24 kpc. H_2CO is an important precursor of CH_3OH , the simplest complex organics, because in cold star-forming cores its formation proceeds on the surface of dust grains via successive hydrogenation of CO ($\text{HCO} \rightarrow \text{H}_2\text{CO} \rightarrow \text{CH}_3\text{O}/\text{CH}_2\text{OH} \rightarrow \text{CH}_3\text{OH}$, e.g. Pauly & Garrod 2018). However, H_2CO can also form in the gas-phase, unlike CH_3OH , in regions where a significant fraction of C is not yet locked into CO (Ramal-Olmedo et al. 2021). If so, H_2CO should form together with species like carbon-chains, which need a large amount of C not locked in CO as well. This implies that in regions where the C/O ratio is smaller, most of the C should be in the form of CO, and carbon-chains should have a lower abundance than that of CH_3OH . The OG is an environment that should have this property, because the [C/H] decrease with R_{GC} is steeper than that of [O/H] (Arellano-Córdova et al. 2020; Méndez-Delgado et al. 2022). The vice-versa is expected in the inner Galaxy. On the other hand, a dust extinction lower in the OG than in the local Galaxy would imply an easier dissociation of CO in gas phase, favouring the formation of carbon chains. From this example, one can see that the formation of even a relatively simple organic molecule like H_2CO , and its relation with CH_3OH , can be different in the outer and inner Galaxy.

The project "CHEMical complexity of star-forming regions in the OUTer Galaxy (CHEMOUT Fontani et al. 2022a,b; Colzi et al. 2022) aims at studying the formation of molecules in the outer Galaxy based on observations of 35 molecular cloud cores associated with star-forming regions having R_{GC} in between 9 and 23 kpc. Using the Institut de Radioastronomie Millimétrique (IRAM) 30m telescope, we detected several simple and complex carbon-bearing molecules including organics ($c\text{-C}_3\text{H}_2$, HCO^+ , H^{13}CO^+ , HCO , C_4H , HCS^+ , HCN , CH_3CCH). Inorganic tracers of star-formation activity (SO , SiO , N_2D^+) were detected as well. The detection of all these species should better constrain their formation/destruction pathways, and highlight similarities and differences with those known to be efficient in the local/inner Galaxy, where the C/O ratio is different. However, the results of Blair et al. (2008), Bernal et al. (2021), and Fontani et al. (2022a,b) are based on observations of single-dish telescopes, and thus provide only abundances averaged over angular scales of their main beams ($\sim 27 - 63''$). At the distance of the CHEMOUT targets, i.e. 8–15 kpc from the Sun (Fontani et al. 2022a), an angular scale of $27''$ corresponds to 1 – 2 pc, or

200 000 – 400 000 au, that is at least a factor 10 larger than the typical linear scale of a single star-forming core (0.05–0.1 pc).

In this work, we present high-angular resolution images obtained with the Atacama Large Millimeter Array (ALMA) to resolve the molecular emission towards the source WB89-670 (IRAS 05343+3605 Wouterloot & Brand 1989), WB670 hereafter. The source is located at a R_{GC} of ~ 23.4 kpc (heliocentric distance ~ 15.1 kpc, Fontani et al. 2022a), in direction of the Galactic anticentre (Galactic coordinates $\text{Lon.}=173.014^\circ$, $\text{Lat.}=2.38^\circ$). This is the CHEMOUT target with the largest Galactocentric distance, thus associated with the smallest environmental [C/H] and [O/H] of the sample, as well as with the lowest C/O ratio (Esteban et al. 2017; Arellano-Córdova et al. 2020; Méndez-Delgado et al. 2022). Extrapolating the elemental Galactocentric gradients of carbon and oxygen measured by Méndez-Delgado et al. (2022) to 23.4 kpc, the fractional abundances [C/H] and [O/H] are 1.8×10^{-5} and 6.7×10^{-5} , respectively. Considering the Solar values of [C/H] $\sim 2.6 \times 10^{-4}$ and [O/H] $\sim 3.1 \times 10^{-4}$, the [C/O] ratio should be ~ 3.1 times lower than Solar in the natal cloud of WB670. The source harbours near- and mid-infrared sources detected in the images of the Two Micron All-Sky Survey (2MASS, Cutri et al. 2003) and the Wide-field Infrared Survey Explorer (WISE, Wright et al. 2010, Fig. 1), associated with molecular gas where rotational transitions of $c\text{-C}_3\text{H}_2$, C_4H , CCS , H^{13}CO^+ , HCO^+ , and HCN (Fontani et al. 2022a), CH_3OH (Bernal et al. 2021), and H_2CO (Blair et al. 2008) were detected. No COMs except CH_3OH were identified in this source. The narrow width at half maximum (about 1 km s^{-1}) in the line profile of $\text{HCO}^+ J = 1 - 0$ suggests that the bulk emission in this transition is from quiescent material, but the simultaneous detection of non-Gaussian wings at high velocities also indicates the presence of embedded protostellar activity (Fontani et al. 2022a).

The paper is organised as follows: the observations and the data reduction are described in Sect. 2. The observational results are shown in Sect. 3. The spectral analysis and derivation of the molecular column densities is illustrated in Sect. 4. A discussion of the results and a comparison with chemical modelling is provided in Sect. 5. Conclusions and future perspectives are given in Sect. 6.

2. Observations and data reduction

The observations were carried out with ALMA during Cycle 9 in three dates: December 27, 2022, using 45 antennas, and January 8 and 9, 2023 (project 2022.1.00911.S, P.I.: F. Fontani), using 41 antennas. The phase centre was set to the equatorial coordinates $\text{R.A.}(J2000)=05\text{h}37\text{m}41.9\text{s}$ and $\text{Dec}(J2000)=36^\circ 07' 22''$. The Local Standard of Rest velocity is -17.4 km s^{-1} (Fontani et al. 2022a). We observed several spectral windows in bands 3 and 4. Information about their central frequencies, spectral resolution, and sensitivity, are given in Table 1. For all the spectral windows, the sources used as flux and bandpass calibrators were J0423-0120 in band 3 and J0854+2006 in band 4, while J0547+2721 and J0550+2326 were used as gain (amplitude and phase) calibrators. The uncertainties in the flux calibration are $\sim 5\%$. The primary beam (i.e. the full width at half maximum of the main beam of a 12m antenna) ranges from $\sim 67''$ at 84.5 GHz to $\sim 57''$ at 99.3 GHz, and from $\sim 41''$ at 140 GHz to $\sim 37''$ at 153.5 GHz.

The calibrated data were produced by the calibration pipeline of the Common Astronomy Software Applications (CASA, McMullin et al. 2007). The pipeline version used is casapipe-6.4.1. Imaging and deconvolution were then performed on the cali-

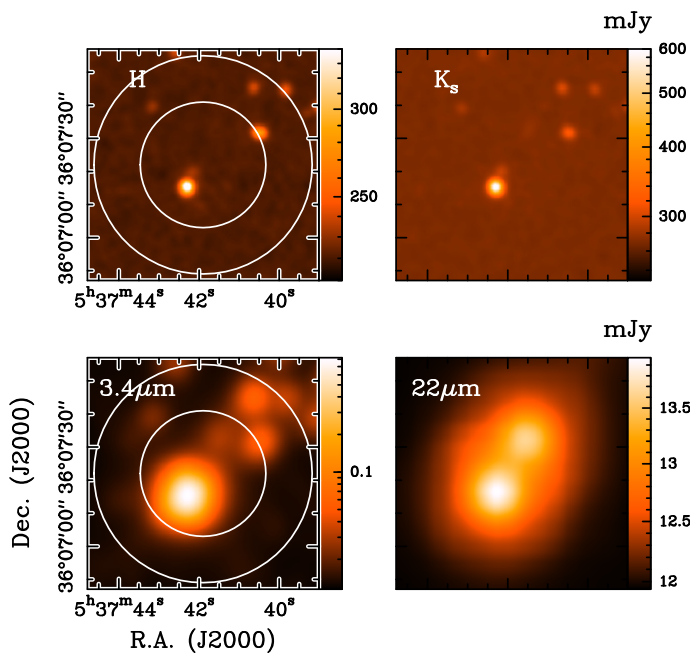


Fig. 1. Near- and mid-infrared images of WB89-670. The top row panels show the images at $1.25 \mu\text{m}$ (H) and $2.15 \mu\text{m}$ (K_s) from the 2MASS survey. The panels in the bottom row show the WISE images at the wavelengths indicated in the top-left corner. The white circles are the ALMA primary beams at ~ 86 GHz and ~ 150 GHz, that are $66''$ (i.e. ~ 7.5 pc) and $38''$ (i.e. ~ 4.3 pc), respectively.

Table 1. Spectral setup and observational parameters.

spw	ν_c^a [GHz]	$\Delta\nu^b$ [kHz]	ΔV^b [km s $^{-1}$]	Chan.	rms c [mJy beam $^{-1}$]
Band 3					
25	84.72719	122	0.43	480	3.9
27	84.52064	122	0.43	480	3.9
29	85.65553	122	0.43	480	3.8
31	85.33839	122	0.43	480	3.9
33	86.64949	488	1.72	1920	1.8
35	97.59944	122	0.38	960	3.6
37	96.79341	122	0.38	960	3.7
39	97.92939	488	1.52	960	1.9
41	99.38944	488	1.52	960	2.0
Band 4					
25	139.75200	488	1.05	1920	8.8
27	141.83430	122	0.26	480	17
29	140.30817	122	0.26	480	17
31	140.80201	122	0.26	960	16
33	151.38080	122	0.24	480	17
35	150.99756	122	0.24	480	18
37	150.50049	122	0.24	960	18
39	153.45220	488	0.96	1920	10

Notes. ^(a) Central frequency of the spectral window (spw); ^(b) Spectral resolution in frequency and velocity; ^(c) Root mean square noise per channel;

brated uv tables with the GILDAS¹ software, after conversion of the calibrated uv tables from measurement sets in uvfits format and then in GILDAS format. To be sensitive to the source extension, the

¹ <https://www.iram.fr/IRAMFR/GILDAS/>

Table 2. Spectral parameters of detected lines.

Quantum Numbers ^a	Rest Freq. (GHz)	$\log[A_{ij}]$ (s $^{-1}$)	E_{up} (K)
$c\text{-C}_3\text{H}_2$			
$J(K_a, K_b) = 2(1, 2) - 1(0, 1)$	85.3389	-4.6341	6.4
HCS ⁺			
$J = 2 - 1$	85.3479	-4.9548	6.1
C ₄ H			
$N = 9 - 8, J = 19/2 - 17/2$			
$F = 9 - 8$	85.6340	-4.8189	20.5
$F = 10 - 9$	85.6340	-4.8163	20.5
$N = 9 - 8, J = 17/2 - 15/2$			
$F = 8 - 7$	85.6726	-4.8217	20.5
$F = 9 - 8$	85.6726	-4.8184	20.5
HCO			
$N_{K_a, K_b} = 1_{0,1} - 0_{0,0}$			
$J = 3/2 - 1/2$			
$F = 2 - 1$	86.6708	-5.3289	4.2
$F = 1 - 0$	86.7084	-5.3377	4.2
$F = 1 - 1$	86.7775	-5.3366	4.2
$F = 0 - 1$	86.8058	-5.3268	4.2
HN ¹³ C			
$J = 1 - 0$	87.0909	-4.7288	4.2
H ¹³ CO ⁺			
$J = 1 - 0$	86.7543	-4.4142	4.2
CH ₃ OH			
$J(K_a, K_b) = 2(1, 2) - 1(1, 1) E_2$	96.7394	-5.5923	12.5
$J(K_a, K_b) = 2(0, 2) - 1(0, 1) A^+$	96.7414	-5.4675	7.0
$J(K_a, K_b) = 2(0, 2) - 1(0, 1) E_1$	96.7445	-5.4676	20.1
³⁴ SO			
$J(K) = 3(2) - 2(1)$	97.7153	-4.9695	9.1
CS			
$J = 2 - 1$	97.9810	-4.7763	7.1
SO			
$J(K) = 3(2) - 2(1)$	99.2999	-4.9488	9.2
H ₂ CO			
$J(K_a, K_b) = 2(1, 2) - 1(1, 1)$	140.8395	-4.2754	21.9
$J(K_a, K_b) = 2(1, 1) - 1(1, 0)$	150.4983	-4.1890	22.6

Notes. ^(a) All spectral parameters are taken from the Cologne Database for Molecular Spectroscopy (CDMS^a; Endres et al. 2016), except those of HCO, which are taken from the Jet Propulsion Laboratory (JPL, Pickett et al. 1998) catalogue;

^a <https://cdms.astro.uni-koeln.de/cdms/portal/>

clean maps were created using natural weighting. As significant emission is detected at the edge of the primary beam, we analyse the primary-beam-corrected images. We attempted to perform self-calibration, but the self-calibrated images did not show any significant improvement due to the faintness of the continuum emission, and hence we analysed the non-self-calibrated images. In the channel maps, the root mean square (rms) varies between 1.8 and 3.9 mJy beam $^{-1}$ in band 3, and between 8.8 and 18 mJy beam $^{-1}$ in band 4. In the continuum images, the rms is ~ 0.025 mJy beam $^{-1}$ in band 3 and ~ 0.1 mJy beam $^{-1}$ in band 4. The angular resolution in both ALMA bands is $\sim 1.4 - 1.5''$, corresponding to ~ 0.1 pc, or ~ 20000 au. In all the images, the maximum recoverable scale is $\sim 20''$. The detected molecular lines and their spectroscopic parameters are listed in Table 2.

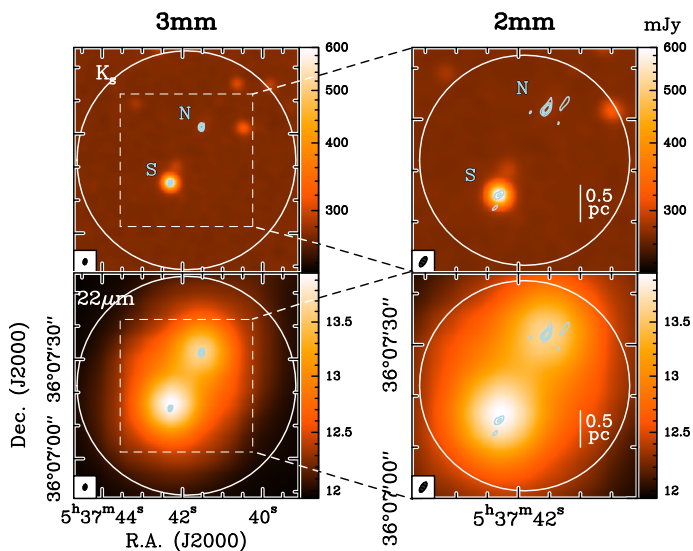


Fig. 2. Continuum emission detected towards WB89-670 with ALMA. The light blue contours in the left and right panels correspond to the 3 mm and 2 mm continuum emission, respectively. Contours start from the 3σ rms level ($\sim 8 \times 10^{-5}$ Jy at 3 mm and $\sim 3 \times 10^{-4}$ Jy at 2 mm), and are in steps of $\sim 5 \times 10^{-5}$ Jy and $\sim 2 \times 10^{-4}$ Jy, respectively. The synthesised beam is depicted in the bottom left corner, and the white circle indicates the ALMA primary beam at the two wavelengths. The region shown in the 2 mm images corresponds to the dashed square illustrated in the top-left panel. The heat colour image in background is the K_s band of 2MASS (Fig. 1) in the top panels, and the WISE $22\mu\text{m}$ band in the bottom panels.

3. Analysis of the maps

3.1. Millimeter continuum emission

The millimeter continuum emission detected towards WB670 in both ALMA bands is shown in Fig. 2. Two compact sources are detected. The strongest one, that we call N, is detected in the 3 mm image with signal-to-noise of 14 (peak flux density $\sim 3.5 \times 10^{-4}$ Jy). Core N is undetected or barely detected in the near-infrared, and it is clearly detected in the mid-infrared. The other one, called S, coincides with the main infrared source detected in all 2MASS and WISE images, and is detected in the 3 mm image with signal-to-noise of 7 (peak flux density $\sim 1.8 \times 10^{-4}$ Jy). The flux densities, F_ν , integrated inside the 3σ rms contour levels are given in Table 3 for both sources, together with other observational properties.

3.2. Spectra extracted from the millimeter continuum sources

The integrated spectra extracted from the contour level at 3σ rms of the 3 mm continuum emission towards cores N and S (Fig. 2) are shown in Fig. 3. The figure shows the detected transitions and the 3σ rms level in the spectra. The chemical richness towards N and S is similar, but the line intensities are overall higher towards N. We will discuss in more detail the chemical differences between the two cores in Sect. 4.1.

3.3. Emission morphology of molecular lines

The molecular transitions listed in Table 2 were detected in some regions of the final images with a signal-to-noise ratio ≥ 5 (the 1σ rms level is in Table 1). For each species, the velocity-integrated emission of the most intense transitions, namely $c\text{-C}_3\text{H}_2$ $J(K_a, K_b) = 2(1, 2) - 1(0, 1)$, H^{13}CO^+ $J = 1 - 0$, CH_3OH

$J(K_a, K_b) = 2(0, 2) - 1(0, 1)\text{A}^+$, CS $J = 2 - 1$, SO $J(K) = 3(2) - 2(1)$, and H_2CO $J(K_a, K_b) = 2(1, 2) - 1(1, 1)$, is shown in Fig. 4. The integration interval in velocity is defined by the channels with signal-to-noise ratio ≥ 3 (see caption of Fig. 4). The other species detected, namely HCS^+ , C_4H , HCO , HN^{13}C , and ^{34}SO , are too faint across the whole mapped region to derive a good integrated map showing their morphology.

Overall, the emission peak of $c\text{-C}_3\text{H}_2$, H^{13}CO^+ , and H_2CO coincides with that of the dust continuum millimeter cores N and S, while that of SO and CH_3OH is located towards a north-western elongated feature that extends for $\sim 20''$ from core N to the north-western border of the primary beam. The emission is extended in all tracers, and shows a filamentary structure oriented SE-NW, whose extension and width depends on the tracer. The filament is narrow in $c\text{-C}_3\text{H}_2$, H^{13}CO^+ , and CH_3OH , and goes roughly from the millimeter core S to the north-western edge of the primary beam. The emission of CS is much broader and arises also from a clump located to the south-eastern edge of the primary beam. This southern clump, extended about $\sim 15''$ in NW-SE direction, is detected also in SO and H_2CO , while is not detected in $c\text{-C}_3\text{H}_2$, H^{13}CO^+ , and CH_3OH . The emission of SO resembles that of CH_3OH in the northern part of the source and around core N, while towards the southern part of the source and around core S is different. The emission of H_2CO is compact and arises mostly from the two millimeter cores, maybe because the E_u of their transitions are higher ($\sim 22 - 23$ K) than those of the other lines ($\sim 4 - 12$ K). The presence of H_2CO in the northern filament cannot be determined because of the limited primary beam, but the integrated emission seems to follow the filament at least inside the primary beam.

To allow for a better inspection of the emission structure of each tracer, the six maps in Fig. 4 are also shown, enlarged, in Figs. A.1–A.6 of Appendix A.

3.4. Spectra extracted from molecular emission regions

The complexity of the source structure described in Sect. 3.3 and the fact that different species emit preferentially in different volumes indicates a chemical differentiation at small spatial scales. Due to this differentiation, we analyse the molecular emission dividing the source in seven regions, based on the emission maps of the species with highest differentiation. The regions are shown in Fig. 4, and are defined roughly on the integrated emission maps of $c\text{-C}_3\text{H}_2$, CH_3OH , SO , and H_2CO : three are based on the dominant clumps detected in $c\text{-C}_3\text{H}_2$ (labelled as 1, 2, and 3 in Fig. 4), one is based on the CH_3OH emission in the north-western filament (4), and one on the southern clump seen in SO (5). To complement the analysis, we also extract spectra from the two dominant clumps detected in H_2CO (6 and 7), which overlap partially with regions 1 and 2 though.

The spectra extracted from these seven regions are shown in Figs. B.1 and B.2. In Table 4, we give the equivalent angular and linear size of the seven regions, derived as the diameter of a circle with the same area. The regions have sizes in between 0.45 and 1.06 pc.

3.5. Comparison between ALMA and IRAM spectra

The $c\text{-C}_3\text{H}_2$, H^{13}CO^+ , and C_4H lines in Table 2 were observed also with the IRAM-30m telescope by Fontani et al. (2022a). To evaluate if extended emission was resolved out by the interferometer, we extracted the integrated ALMA spectra in flux density units of the mentioned lines from a circular region with size

Table 3. Parameters of the millimeter continuum sources

Core	R.A. <i>h : m : s</i>	Dec. <i>° : ′ : ″</i>	$F_{\nu,3\text{mm}}^a$ Jy	$F_{\nu,2\text{mm}}^a$ Jy	θ_s^b ″	D^c pc	$N(\text{H}_2)^d$ $\times 10^{21} \text{cm}^{-2}$	M_d^d M_\odot	$n(\text{H}_2)^d$ $\times 10^4 \text{cm}^{-3}$	β^e
N	05:37:41.55	36:07:31.9	3.0×10^{-4}	8.3×10^{-4}	2.4	0.18	5.7(1.2)	2.9(1.5)	1.1	0.34
S	05:37:42.31	36:07:15.2	1.4×10^{-4}	3.9×10^{-4}	2.0	0.15	2.1(0.5)	0.7(0.4)	0.5	0.21

Notes. ^(a) Flux density integrated in the 3σ rms level; ^(b) Deconvolved angular diameter; ^(c) Deconvolved linear diameter; ^(d) H_2 mass computed from the dust thermal continuum emission as described in Sect 4.2, assuming a dust temperature equal to the excitation temperature of CH_3OH (Table 5), and a dust mass opacity coefficient $\beta = 1.7$; ^(e) Dust opacity index computed comparing the integrated flux densities at the two frequencies observed as described in Sect 4.2.

Table 4. Angular and linear size of the seven molecular emitting regions shown in Fig. 4.

Region	θ_s ″	D_s pc
<i>c</i> - C_3H_2		
1	11.6	0.85
2	7.5	0.55
3	8.3	0.61
CH_3OH		
4	14.5	1.06
SO		
5	12.9	0.94
H_2CO		
6	6.1	0.45
7	9.5	0.69

equal to that of the IRAM 30m telescope main beam ($\sim 27''$). Then, we converted the IRAM 30m spectra from main beam temperature units to flux density units through the equation (see e.g. Fontani et al. 2021):

$$F_\nu[\text{mJy}] = \frac{T_{\text{MB}}[\text{K}]}{1222} \nu[\text{GHz}]^2 \Theta[']^2, \quad (1)$$

where F_ν is the flux density at the observed rest frequency ν , T_{MB} is the main beam temperature, and Θ the main beam angular size of the IRAM 30m telescope at frequency ν .

The comparison is shown in Fig. 5. The flux densities measured with ALMA are consistent with those measured with the IRAM-30m telescope in *c*- C_3H_2 and H^{13}CO^+ within a factor $\leq 10\%$, fully consistent with the calibration errors. For C_4H , we show in Fig. 5 the $J = 19/2 - 17/2$ hyperfine component, for which the difference between the IRAM and ALMA spectra is the largest (a factor $\sim 1.3 - 1.4$). Considering the calibration errors and the rms noise in the spectra (in particular in the C_4H IRAM 30m spectrum), we conclude that the amount of extended flux resolved out by ALMA is negligible and does not affect significantly our analysis.

4. Spectral analysis and derivation of column densities

4.1. Spectral analysis

Flux densities were converted to brightness temperatures (T_{B}) according to Eq. 1. This relation needs the observed angular equivalent diameter (i.e. the diameter of the equivalent circle) of each core. Therefore, T_{B} is an average brightness temperature over the solid angle of each core. We have analysed the

spectra in T_{B} units with the MADrid Data CUBe Analysis (MADCUBA², Martín et al. 2019) software. The transitions reported in Table 2 were modelled via the Spectral Line Identification and LTE Modelling (SLIM) tool of MADCUBA. The lines were fitted with the AUTOFIT function of SLIM. This function produces the synthetic spectrum that best matches the data assuming a constant excitation temperature (T_{ex}) for all transitions of the same species. The other input parameters are: total molecular column density (N_{tot}), radial systemic velocity of the source (V), line full-width at half-maximum (FWHM), and angular size of the emission (θ_s). AUTOFIT assumes that V , FWHM, and θ_s are the same for all transitions. For θ_s , we assumed that the emission is more extended than the extraction region in all tracers, and hence no filling factor is applied in the derivation of the best fit parameters. Assuming as θ_s the equivalent radii given in Table 4 would change the resulting column densities by at most a factor 1.2. We left all other parameters free except T_{ex} , that we had to fix for all species except CH_3OH , which is the only molecule for which two transitions with significantly different E_u were detected (Table 2). We decided to adopt for all species the T_{ex} measured from CH_3OH .

The analysis described above with MADCUBA was adopted for the lines of these species: *c*- C_3H_2 , CH_3OH , H_2CO , C_4H , and HCS^+ . For the remaining ones, namely HCO , H^{13}CO^+ , HN^{13}C , CS , SO , and ^{34}SO , MADCUBA cannot fit the lines in all regions because the observed FWHMs are comparable to the spectral resolution of their spectra (spw 33, 39, and 41 in Band 3). Towards region 5, CH_3OH could also not be fit for the same reason. Therefore, for these species, we obtained the integrated intensities of the lines with the CLASS³ package of the GILDAS software. N_{tot} were then calculated with the same equations used by MADCUBA, namely assuming LTE at T_{ex} equal to that derived from CH_3OH also in this case. We assumed also optically thin conditions. The assumption is justified both by the Gaussian line profiles, and by the fact that the optical depths provided by AUTOFIT for the lines analysed with MADCUBA are consistent with optically thin conditions.

The results obtained are listed in Table 5. One remarkable immediate result is the small values of the FWHMs of all lines, which are narrower than $\sim 2 \text{ km s}^{-1}$ both in N and S. Even though the cores harbour infrared-bright sources, the FWHMs are narrow and comparable to those measured in starless cores in infrared dark clouds (e.g. Kong et al. 2017; Barnes et al. 2023) rather than to those measured in infrared-bright protostellar envelopes (e.g. Fontani et al. 2002, 2023). The excitation temperatures derived from CH_3OH are $\sim 9 \text{ K}$ and $\sim 15 \text{ K}$ in core N

² MADCUBA is a software developed in the Madrid Center of Astrobiology (INTA-CSIC) which enables to visualise and analyse single spectra and data cubes. <https://cab.inta-csic.es/madcuba/>

³ <https://www.iram.fr/IRAMFR/GILDAS/doc/pdf/class.pdf>

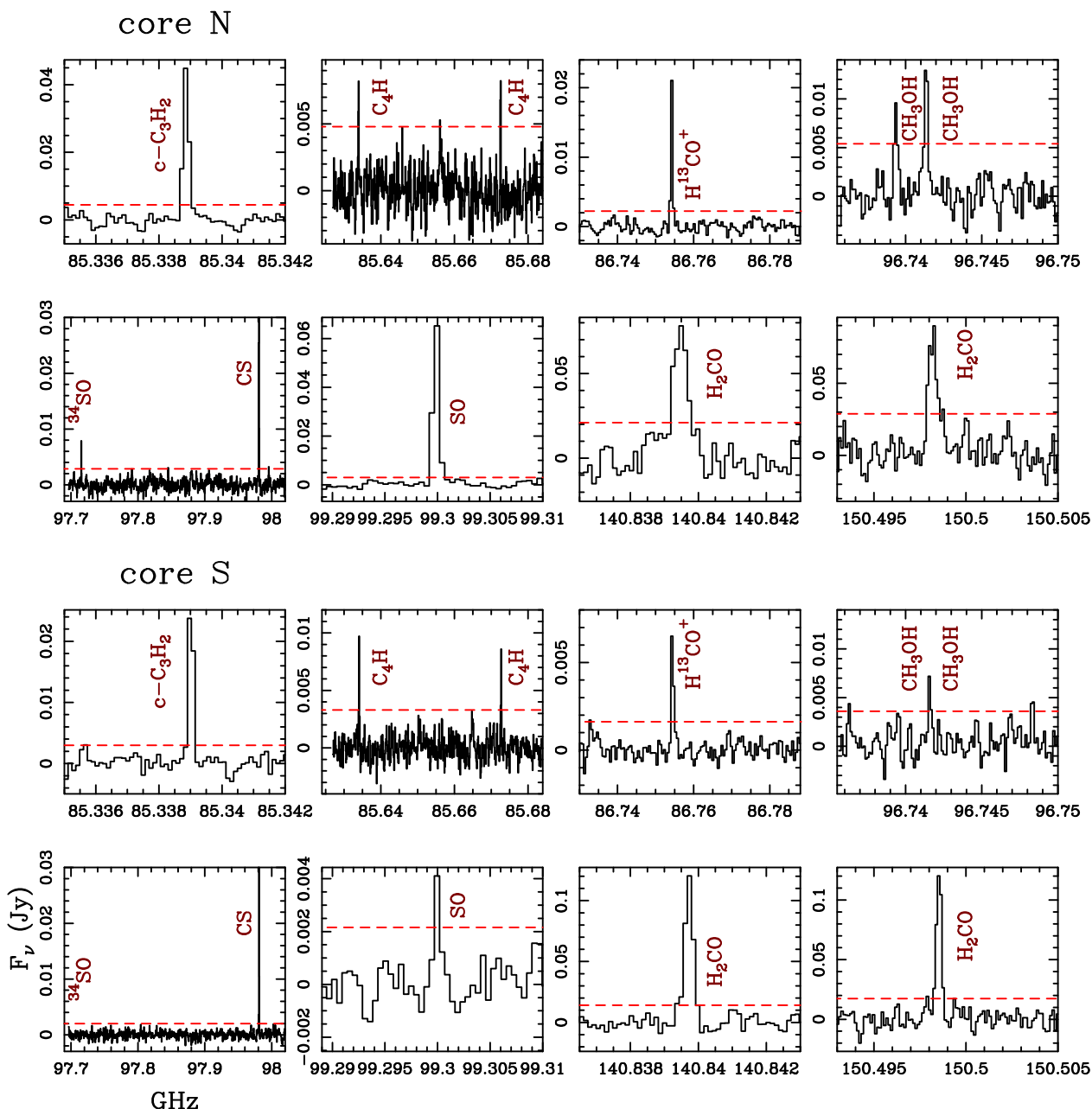


Fig. 3. Spectra extracted from the 3σ rms level contour of the 3 mm continuum for cores N (top) and S (bottom) (Fig. 2). In the eight spectral windows, the clearly detected transitions are labelled, and the 3σ rms level is represented by the red dashed line. The undetected species, namely HCS^+ , HCO and HN^{13}C , are not shown.

and S, respectively. Such low temperatures could indicate sub-thermal excitation conditions, at least for CH_3OH . Assuming the same T_{ex} for the other molecules, as explained above, we derived N_{tot} of the order of $\sim 10^{12} \text{ cm}^{-2}$ for H^{13}CO^+ , and of the order of $\sim 10^{13} \text{ cm}^{-2}$ for CH_3OH , C_4H , H_2CO , CS , and SO .

As stated above, to derive N_{tot} we fixed T_{ex} to that of CH_3OH for all molecules. This assumption is justified by the fact that all transitions analysed have energies of the upper level in between ~ 4 and ~ 20 K, similar to the energy range of the methanol lines (7–20 K). However, the computed low T_{ex} could indicate sub-thermal conditions for CH_3OH . We estimate the uncertainty introduced by this simplified approach varying T_{ex} in between the CH_3OH values and a representative kinetic temperature of the gaseous envelope of high-mass protostellar objects ~ 30 K (e.g. Sánchez-Monge et al. 2013; Fontani et al. 2015), in case

CH_3OH emission is sub-thermally excited. The N_{tot} variation is dependent of the species and it is on average larger for core N, for which the difference between T_{ex} from CH_3OH (9 K) and the representative temperature of 30 K is the highest. For example: in core N, N_{tot} of CS increases from 1.7×10^{13} to $2.6 \times 10^{13} \text{ cm}^{-2}$; N_{tot} of H^{13}CO^+ increases from 1.5×10^{12} to $2.8 \times 10^{12} \text{ cm}^{-2}$; $c\text{-C}_3\text{H}_2$ cannot be reasonably fit with a T_{ex} above 15 K, if one considers both the detected transition and the upper limit on the transition $J(K_a, K, b) = 4(3, 2) - 4(2, 3)$, at ~ 85.656 GHz but undetected; N_{tot} of C_4H decreases from 9.1×10^{12} to $5.5 \times 10^{12} \text{ cm}^{-2}$; N_{tot} of H_2CO remains the same within the errors.

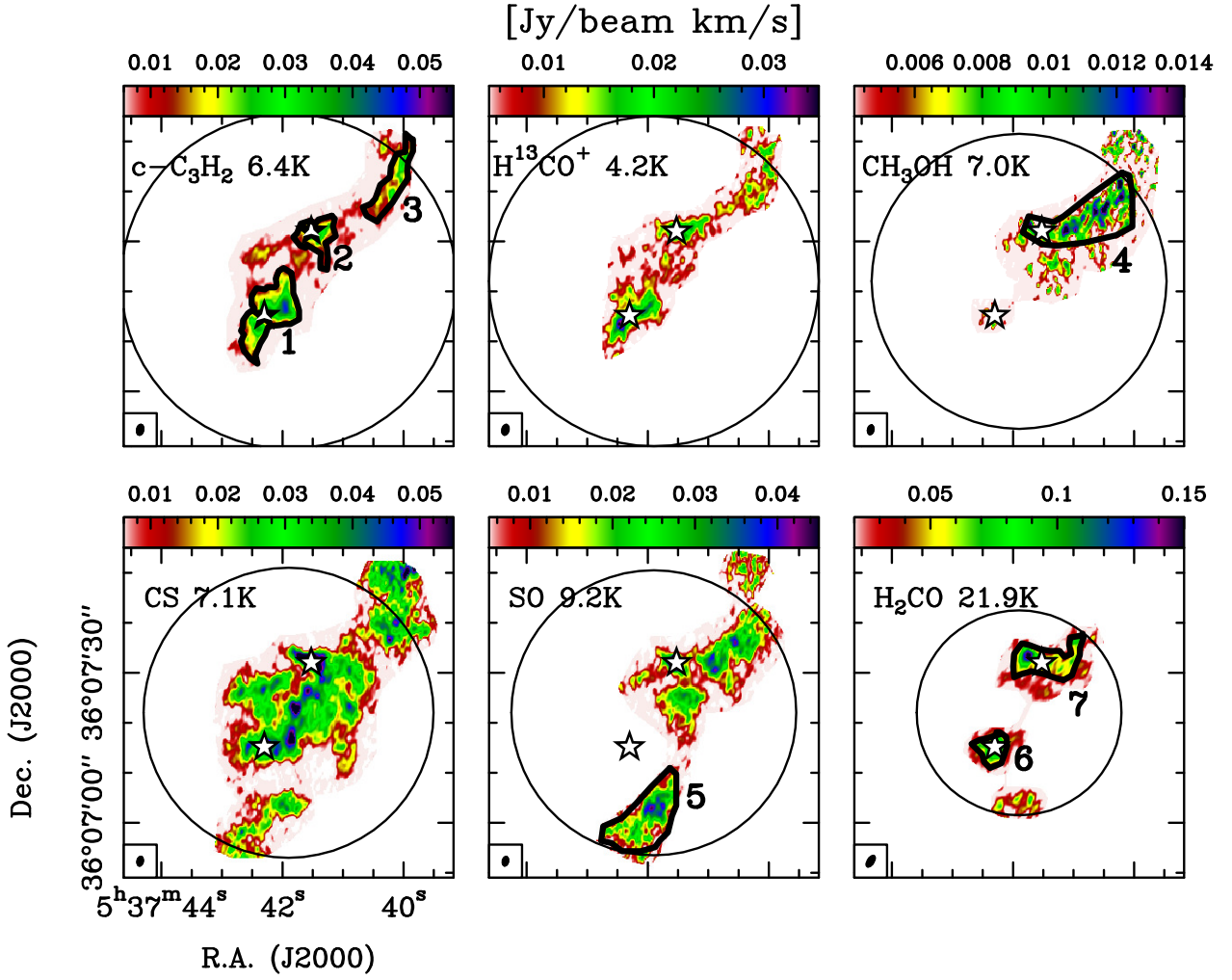


Fig. 4. Velocity-integrated molecular emission maps. We show the six molecular species for which the signal-to-noise ratio is good. For C_4H , HCS^+ , HCO , $HN^{13}C$, and ^{34}SO , the maps are too noisy and we do not show them. The species, and the E_{up} of the line used in temperature units, are indicated in the top-left corner of each frame. The two stars indicate the peak position of the millimeter continuum cores N and S. The black circles highlight the primary beam at the rest frequency of each line (Table 2). The integrated emission was computed in the channels with intensity higher than the 3σ rms level. The velocity intervals used are: $[-18.4; -16.5]$ $km\ s^{-1}$ for $c-C_3H_2$; $[-19; -16]$ $km\ s^{-1}$ for $H^{13}CO^+$; $[-18.75; -16; 25]$ $km\ s^{-1}$ for CH_3OH (from the line centred at ~ 96.7414 GHz) at $[-20; -14]$ $km\ s^{-1}$ for CS; $[-19.5; -15.5]$ $km\ s^{-1}$ for SO; $[-18.8; -16.2]$ $km\ s^{-1}$ for H_2CO (from the line centred at ~ 140.8395 GHz). The seven regions highlighted in black are those analysed in detail in Sect. 3.4, and correspond grossly to the 5σ rms emission contour of the corresponding integrated intensity map (within the ALMA primary beam).

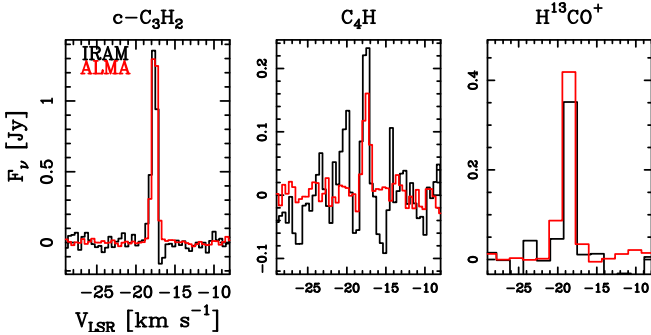


Fig. 5. Flux density comparison between ALMA and IRAM 30m spectra. The IRAM 30m and ALMA spectra are shown as black and red histograms, respectively. The ALMA spectra were extracted from an angular region equivalent to the IRAM 30m beam at the frequency of the lines ($\sim 27''$).

4.2. Fractional abundances in the continuum cores

To estimate the molecular fractional abundances with respect to H_2 , we compute the column density of H_2 , $N(H_2)$, from the integrated continuum flux density through the equation (e.g. Battersby et al. 2014):

$$N(H_2) = \frac{\gamma F_\nu}{\Omega \kappa_\nu B_\nu(T_d) \mu(H_2) m_H}, \quad (2)$$

where γ is the gas-to-dust mass ratio, F_ν is the flux density at frequency ν , Ω is the source solid angle at the observed frequency, κ_ν is the dust opacity usually parametrised as $\kappa_\nu = \kappa_{\nu_0} (\nu/\nu_0)^\beta$ (Ossenkopf & Henning 1994), $B_\nu(T_d)$ is the Planck function at dust temperature T_d , $\mu(H_2)$ is the mean molecular weight for which we will adopt 2.8 (Kauffmann et al. 2008), and m_H is the mass of the hydrogen atom. Using the empirical relation between γ and R_{GC} derived from Giannetti et al. (2017), we find $\gamma \sim 3000$ at $R_{GC} = 23.4$ kpc. Considering the uncertainties in the Giannetti et al. (2017) empirical relation, γ is 3000^{+700}_{-2200} , hence more than 8 times higher than the conventional value of

100. We adopt for T_d the excitation temperature derived from CH₃OH (Table 5) for each core, assuming coupling between gas and dust. We also assume dust opacity index $\beta = 1.7$, a typical value used for ice-coated dust grains in dense cores, and $\kappa_{\nu_0} = 0.899$ at $\nu_0 = 230$ GHz (Ossenkopf & Henning 1994). The resulting $N(\text{H}_2)$ are $\sim 5.7 \times 10^{21}$ and $\sim 2.1 \times 10^{21} \text{ cm}^{-2}$, respectively. Assuming spherical sources, we also compute the core H₂ gas masses, M_d , and volume densities, $n(\text{H}_2)$. M_d and $n(\text{H}_2)$ are of the order of $\sim 1 M_\odot$ and of $\sim 10^4 \text{ cm}^{-3}$, respectively, for both cores, with core N being more dense and massive. All parameters are listed in Table 3. We show the molecular fractional abundances derived from the $N_{\text{tot}}\text{-to-}N(\text{H}_2)$ ratio in Table 5.

These estimates are affected by several uncertainties. First, as discussed in Sect. 4.1, N_{tot} can vary up to a factor 2 depending on the species. Second, computing β from the integrated continuum flux densities in the 3 mm and 2 mm bands (Tab. 3) through Eq.(2) in Chacón-Tanarro et al. (2019b), we find $\beta \sim 0.34$ and $\beta \sim 0.21$ for core N and S, respectively. With these β , we find $N(\text{H}_2) \sim 1.6 \times 10^{21} \text{ cm}^{-2}$ for N and $N(\text{H}_2) \sim 1.6 \times 10^{21} \text{ cm}^{-2}$ for S, respectively, i.e. a factor ~ 3 smaller than those given in Table 3. The molecular abundances in Table 5, hence, would increase systematically by the same factor. Another big uncertainty is introduced by the value of $\gamma = 3000^{+700}_{-2200}$ calculated from Giannetti et al. (2017), which makes the abundances to vary up to an additional factor ~ 4 . There are also the uncertainties on β , which depend on the measured continuum flux densities and dust temperatures. While the relative error on the continuum flux densities is $\sim 10\%$, that on the dust temperature is difficult to quantify. However, we stress that all these uncertainties affect the individual abundances but not their ratios.

In the diffuse ISM, β is ~ 2 (e.g. Draine & Lee 1984), while lower values are measured in dense cores (e.g. Forbrich et al. 2015; Galametz et al. 2019) and circumstellar discs (e.g. Testi et al. 2014; Friesen et al. 2018). β can depend a lot on grain size, composition, and porosity, but values lower than 0.5 are hard to explain without considering large grains of size $\sim 100 \mu\text{m} - 1 \text{ mm}$ (e.g. Testi et al. 2014; Ysard et al. 2019). In protoplanetary discs, such large grains are expected as a result of coagulation and growth. However, cores N and S have a linear diameter $\geq 30000 \text{ au}$, hence the observed emission is unlikely dominated by a circumstellar disc. Values of β lower than 1 were measured also up to $\sim 2000 \text{ au}$ scales around young protostars (e.g. Galametz et al. 2019), indicative of early grain growth, although theory is struggling in finding the possible reasons for such growth at the relatively low density of the 1000 – 10000 au scale of protostellar envelopes. It has been proposed that large grains are not formed on such extended envelope scales, but transported there from the site of growth via jets and winds (e.g. Cacciapuoti et al. 2024). This scenario could be possible for WB670, but the narrow FWHMs of the observed lines in N and S (Tab. 5) suggest a very quiescent environment, and hence should be disregarded. Silsbee et al. (2022) proposed that the presence of very small grains could also cause a low β . This scenario may be possible if the distribution of grain size at the Galactocentric distance of WB670 is different from that in the local medium. Other options are also possible, like high dust opacities, and contamination from free-free emission at 3 mm. We did not find in the literature any free-free emission study towards WB670 (e.g. from radio-continuum emission), and hence this option cannot be checked.

Table 5. Best-fit parameters of the millimeter continuum sources N and S spectra.

molecule	V km s^{-1}	FWHM km s^{-1}	T_{ex} K	N_{tot} $\times 10^{12} \text{ cm}^{-2}$	$[\text{X}]^a$ $\times 10^{-9}$
N					
<i>c</i> -C ₃ H ₂	-17.40(0.01)	0.74(0.02)		7.9(0.2)	1.4
HCS ⁺	–	–		≤ 0.4	≤ 0.07
C ₄ H	-17.32(0.05)	0.9(0.1)		19(2)	3.3
HCO	–	–		≤ 3.2	≤ 0.6
HN ¹³ C	–	–		≤ 0.3	≤ 0.05
H ¹³ CO ⁺	-17.37(0.07)	2.01(0.08)		1.5(0.1)	0.3
CH ₃ OH	-17.4(0.1)	0.92(0.08)	9(2)	2.2(0.3)	0.4
CS	-17.46(0.03)	2.00(0.04)		17(2)	3.0
SO	-17.44(0.02)	2.01(0.05)		43(1)	7.5
H ₂ CO	-17.37(0.04)	1.25(0.09)		8.5(0.5)	1.5
S					
<i>c</i> -C ₃ H ₂	-18.0(0.1)	0.7(0.1)		7.6(0.8)	3.6
HCS ⁺	–	–		≤ 0.6	≤ 0.3
C ₄ H	-17.93(0.03)	0.69(0.06)		44(4)	21
HCO	–	–		≤ 2.1	≤ 1
HN ¹³ C	–	–		≤ 0.4	≤ 0.2
H ¹³ CO ⁺	-18.0(0.6)	1.6(1)		1.0(0.3)	0.5
CH ₃ OH	-18.0(0.7)	1.1(0.5)	15(3)	23(3)	11
CS	-17.92(0.02)	1.87(0.03)		11.7(1)	5.6
SO	-17.8(0.2)	2.1(0.4)		3.4(0.8)	1.6
H ₂ CO	-17.96(0.01)	0.63(0.03)		8.5(0.8)	4.0

Notes. ^(a) Fractional abundance with respect to H₂, computed as $N_{\text{tot}}/N(\text{H}_2)$. $N(\text{H}_2)$ is calculated from the continuum flux density in Table 3 as explained in Sect. 4.2.

4.3. Column densities in the molecular emitting regions

In Appendix C, we list the parameters obtained fitting the lines with MADCUBA and CLASS towards the lines detected in the seven regions indicated in Fig. 4. As for the continuum cores, the FWHMs are always narrower than 1.5-2 km s⁻¹, indicating quiescent gas. The T_{ex} derived from the two detected CH₃OH lines are in between 6.4 K and 15 K, similar to that measured towards cores N and S, suggesting that the emission arise from cold gas also in these regions. This is consistent again with the relatively low FWHMs of the lines, smaller than $\sim 1 - 2 \text{ km s}^{-1}$, which indicates further that the emission arise from quiescent material. Regarding N_{tot} , for CH₃OH we derive values of the order of $10^{12} - 10^{13} \text{ cm}^{-2}$, with the maximum value ($\sim 1.6 \times 10^{13} \text{ cm}^{-2}$) in the north-western filament in between core N and the edge of the primary beam. The hydrocarbons C₄H and *c*-C₃H₂ have similar column densities, both of the order of $\sim 10^{12} \text{ cm}^{-2}$. For these regions we cannot derive abundances because we cannot estimate the H₂ column densities, hence we will discuss the comparison between the N_{tot} of the various species in Sect. 5.1.

5. Discussion

5.1. Column density comparisons

In Fig. 6 we compare the molecular column densities between different species in the seven regions of WB670. The relative N_{tot} of the hydrocarbons C₄H and *c*-C₃H₂ are similar and do not change significantly in the sub-regions of WB670, as shown in panel (a) of Fig. 6. Both species require atomic C not locked in CO to form, therefore their good agreement in the different re-

gions is consistent with the expectations. In panel (b) of Fig. 6 we compare N_{tot} of H_2CO , HCO , and CH_3OH , which are thought to be chemically related because all can be formed from hydrogenation of CO on dust grains. N_{tot} of CH_3OH is largely variable in the seven sub-regions, and the trend does not follow that of HCO and H_2CO , since the higher N_{tot} of CH_3OH are found where those of HCO and H_2CO are lower, and vice versa.

The same dichotomy is apparent also between CH_3OH and $c\text{-C}_3\text{H}_2$ (panel (c)), especially evident in region 1, where N_{tot} of CH_3OH is the lowest and that of $c\text{-C}_3\text{H}_2$ is the highest, and in region 4, where the opposite happens. A similar dichotomy is observed in the pre-stellar core L1544 (Spezzano et al. 2016; Jensen et al. 2023), where the emission of the two molecules seems anti-correlated. In particular, CH_3OH emission arises from colder and more shielded regions of the L1544 core envelope, while $c\text{-C}_3\text{H}_2$ emission overlaps with the dust continuum emission. Such observational difference is consistent with the different physical conditions needed to form the two molecules. While it is well-known that CH_3OH is formed from sequential hydrogenation of CO on grain surfaces (e.g. Fuchs et al. 2009), the formation of $c\text{-C}_3\text{H}_2$ occurs in the gas-phase through an ion-molecule reaction followed by dissociative recombination (e.g. Sipilä et al. 2016). These reactions do not need a low-temperature and high-density environment like that required for CH_3OH formation. Therefore, the dichotomy between these two species likely arises from such different formation routes. Interestingly, the variation of N_{tot} in the seven regions found for H_2CO and HCO (panel (b) in Fig. 6) resembles more that of $c\text{-C}_3\text{H}_2$ than that of CH_3OH . This points to formation routes of H_2CO and HCO in gas-phase rather than from surface chemistry processes. In particular, while CH_3OH can be formed only on the surfaces of dust grains given the inefficiency of gas phase routes at low temperatures (e.g. Garrod et al. 2006), H_2CO is also known to form in the gas phase from regions rich in hydrocarbons, where C is not yet completely locked in CO (see e.g. Chacón-Tanarro et al. 2019a). HCO can also form via gas-phase reactions (Rivilla et al. 2019). Our observations seem to indicate that the gas-phase formation of H_2CO and HCO from atomic C is likely more efficient than its formation on dust grains, despite the lower abundance of C at such large Galactocentric distances.

The trends of the molecular ions H^{13}CO^+ and HCS^+ are also more in line with hydrocarbons and H_2CO rather than with CH_3OH (panels (d) and (e)). Again, this can be attributed to a formation of these ions only in gas-phase. The species for which the trend in N_{tot} is the most similar to CH_3OH is SO, as indicated in panel (f) of Fig. 6. This similarity could be explained by their common origin from surface chemistry. In fact, SO is thought to be formed in gas phase from atomic S (e.g. Vidal et al. 2017), more abundant upon grain sputtering than in the diffuse gas.

5.2. Comparison with local and inner Galaxy star-forming regions

Extrapolating the elemental abundance trends measured by Méndez-Delgado et al. (2022) at the Galactocentric distance of WB670, the oxygen, carbon, and nitrogen fractional abundances should be: $[\text{O}/\text{H}] \sim 6.7 \pm 2.3 \times 10^{-5}$, $[\text{C}/\text{H}] \sim 1.8 \pm 0.5 \times 10^{-5}$, and $[\text{N}/\text{H}] \sim 5.3 \pm 1.3 \times 10^{-6}$, respectively. The reference values at the Solar circle are: $[\text{O}/\text{H}] \sim 3.1 \pm 1.0 \times 10^{-4}$, $[\text{C}/\text{H}] \sim 2.6 \pm 0.8 \times 10^{-4}$, and $[\text{N}/\text{H}] \sim 4.7 \pm 1.4 \times 10^{-5}$, respectively (Méndez-Delgado et al. 2022). Therefore, the relative elemental ratios $[\text{O}/\text{C}]$ and $[\text{O}/\text{N}]$ should increase from $[\text{O}/\text{C}] \sim 1.2 \pm 0.7$ and $[\text{O}/\text{N}] \sim 6.6 \pm 4.0$ to $[\text{O}/\text{C}] \sim 3.7 \pm 2.0$ and $[\text{O}/\text{N}] \sim 12.6 \pm 7.6$. A molecular ratio that, in principle, can be particularly sensitive to changes in the $[\text{O}/\text{C}]$

ratio is $\text{CH}_3\text{OH}/c\text{-C}_3\text{H}_2$ as found in the pre-stellar core L1544 (e.g. Spezzano et al. 2016), since to form CH_3OH one needs carbon locked in CO and to form $c\text{-C}_3\text{H}_2$ one needs free atomic carbon. Figure 7 shows the column density ratios $\text{CH}_3\text{OH}/c\text{-C}_3\text{H}_2$ in the seven molecular regions of WB670, and compare them to the ratios measured in local (low- and high-mass) star-forming regions (Higuchi et al. 2018) and in the outer Galaxy hot-core WB89-789 (hereafter WB789, Shimonishi et al. 2021). As representatives of local low-mass star-forming regions, we took the cores in the Perseus molecular clouds observed by Higuchi et al. (2018). As representatives of high-mass star-forming regions, we took IRAS 20126 and AFGL 2591 (Freeman et al. 2023). The linear scale resolved is $\sim 5000 - 10000$ au in Higuchi et al. (2018), while it is ~ 200000 au in (Freeman et al. 2023). The $\text{CH}_3\text{OH}/c\text{-C}_3\text{H}_2$ ratios derived in WB670 agree on average with the lower values measured in local star-forming regions, while the ratio found in WB789 is twice the highest local values (Fig. 7). Because WB789 is located in between the local Galaxy and WB670, there does not seem to be a monotonic trend of the $\text{CH}_3\text{OH}/c\text{-C}_3\text{H}_2$ ratio with the Galactocentric distance. We will better discuss the comparison between WB670 and WB789 in Sect. 5.3.

We also checked if the column density ratios we derive in WB670 between species that differ from just one element such as HN^{13}C and H^{13}CO^+ , and CS and SO, can eventually be attributed to the change in elemental ratios with R_{GC} . Figure 8 shows the column density ratios SO/CS (panel (a)). Despite a dispersion of an order of magnitude, the average value is $\text{SO}/\text{CS} \sim 1.2$. Fontani et al. (2023) found average $\text{SO}/^{13}\text{CS}$ ratios $\sim 11 - 12$ in a sample of high-mass star-forming cores in different evolutionary stages, and in the local and inner Galaxy. This ratio translates into ~ 0.2 when considering a conversion factor $^{12}\text{C}/^{13}\text{C} \sim 68$ for the local ISM (Milam et al. 2005) (dashed line in panel (a) of Fig. 8). Scaling this value for the increase in the $[\text{O}/\text{C}]$ elemental ratio (~ 3.1) from the Solar circle to $R_{\text{GC}} \sim 23.4$ kpc (Méndez-Delgado et al. 2022), the expected $[\text{SO}/\text{CS}]$ column density ratio in WB670 should be ~ 0.62 , that is a factor 2 smaller than the average measured one. But the dispersion is such that, overall, the measured ratios are consistent with those measured in the Solar neighbourhoods scaled for metallicity. Panel (b) of Fig. 8 shows the $\text{H}^{13}\text{CO}^+/\text{HN}^{13}\text{C}$ column density ratios measured in WB670. The average value is ~ 2.6 . In this case the dispersion is only a factor ~ 2 . In local and inner Galaxy star-forming regions this molecular ratio is very variable. Vasyunina et al. (2011) measured an average HCO^+/HNC ratio of ~ 10 in infrared-dark clouds. Zinchenko et al. (2009) found $\text{H}^{13}\text{CO}^+/\text{HN}^{13}\text{C} \sim 1$ in a sample of high-mass star-forming regions, indicating that this ratio can be very sensitive to changes in the physical conditions. Because WB670 contains infrared-bright objects, its physical conditions are likely similar to those of the active star-forming regions observed by Zinchenko et al. (2009). This means that the observed $\text{H}^{13}\text{CO}^+/\text{HN}^{13}\text{C}$ column density ratio increases on average by a factor 2.6 from local star-forming regions to $R_{\text{GC}} \sim 23.4$ kpc, while the expected increase of the $[\text{O}/\text{N}]$ elemental ratio should be ~ 1.8 . Therefore, again the increased elemental abundance ratio cannot fully explain the observed molecular ratios. However, considering the dispersion of the values in the literature, and the error introduced by the assumed T_{ex} in our analysis, overall the ratios are consistent with a metallicity-scaled trend. On the other hand, the elemental ratios beyond $R_{\text{GC}} \sim 15$ kpc are poorly constrained by observations (e.g. Romano et al. 2020) and suffer from uncertainties up to $\sim 30\%$ on the individual elemental abundances (Méndez-

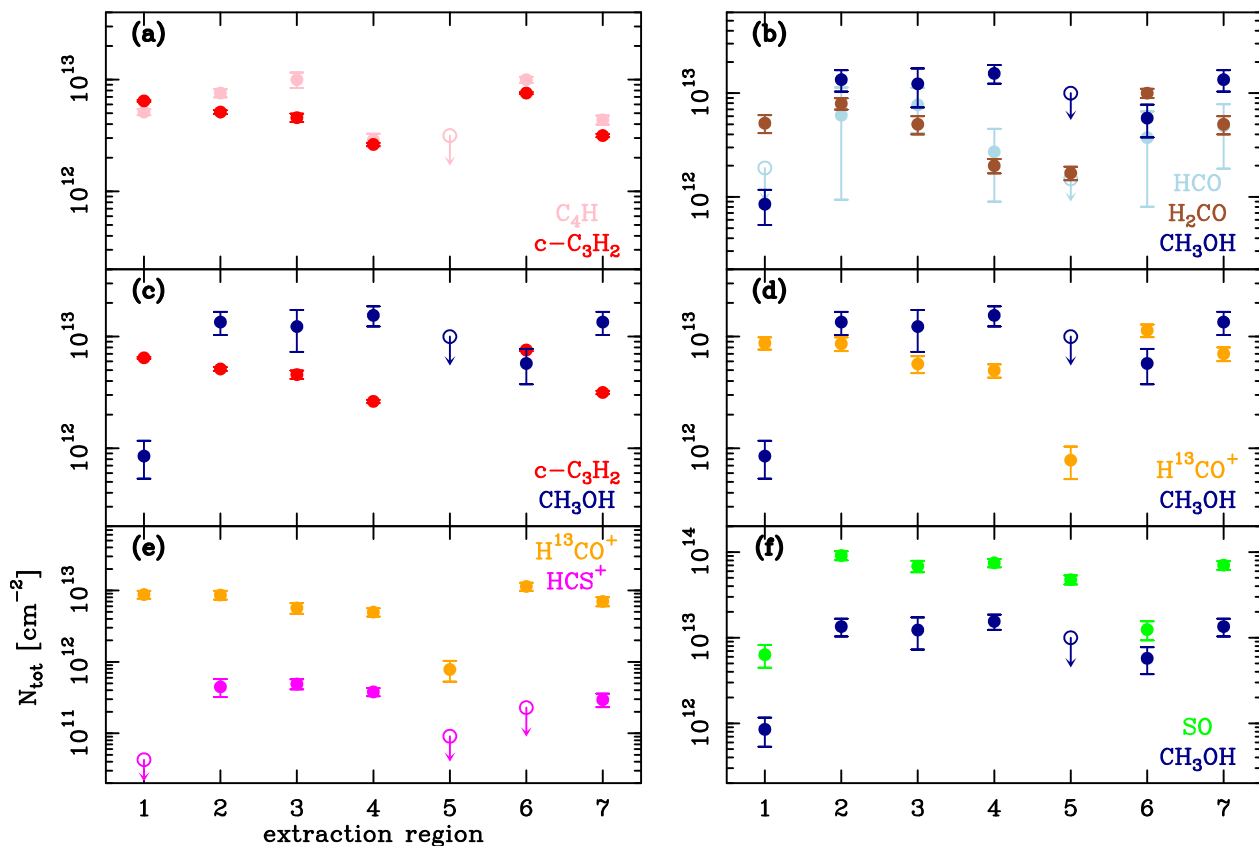


Fig. 6. Column density comparison in the seven molecular extraction regions. The colours in the different panels indicate the different molecular species according to the labels in the bottom-right corner (top-right corner in panel (e)). Empty symbols with an arrow pointing downwards are upper limits.

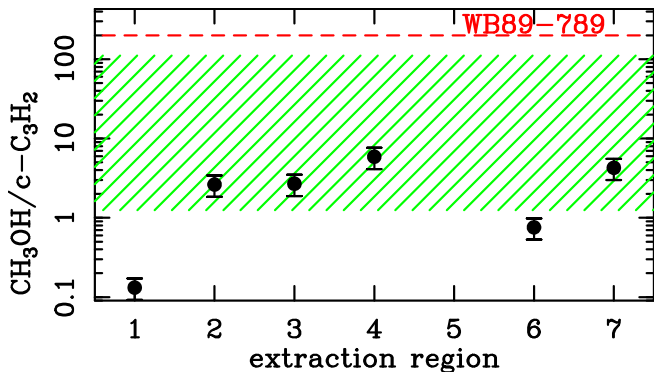


Fig. 7. Column density ratio $\text{CH}_3\text{OH}/c\text{-C}_3\text{H}_2$ in WB670 and other star-forming regions. The black points indicate the ratios measured in the seven regions of WB670 (with the exception of region 5, for which both column density estimates are upper limits). The green area correspond to the range of values measured in local star-forming regions (Higuchi et al. 2018), and the red dashed line is the ratio measured in the outer Galaxy hot-core WB789 (Shimonishi et al. 2021).

Delgado et al. 2022), and hence their extrapolation to such large R_{GC} could be inaccurate.

5.3. Comparison with sub-Solar metallicity hot-cores

Some species detected in WB670 were also detected in the hot core WB789 (Shimonishi et al. 2021), located at $R_{\text{GC}} \sim 19$ kpc. The species in common are: $c\text{-C}_3\text{H}_2$, CH_3OH , H_2CO , H^{13}CO^+ , SO , and CS . Shimonishi et al. (2021) derive two abundance val-

ues, computed on linear diameters of 0.026 and 0.1 pc, respectively. For the comparison with N and S, we use the 0.1 pc values because this size is more similar to that of N and S (Table 3). Figure 9 shows the comparison: except for SO , all other species show abundances significantly different from each other, indicating a clear different chemical composition. In particular, the CH_3OH abundance in WB789 is two orders of magnitude higher than in N and S, while the abundances of all other carbon-bearing species are lower. In fact, the CH_3OH abundance in WB789 is 2×10^{-7} , while in N and S is 0.4×10^{-9} and 11×10^{-9} , respectively. Even considering the abundances obtained assuming β in Table 3, that are a factor ~ 3 higher than those listed in Table 5, the CH_3OH abundances in N, S, and WB789 are not consistent. Shimonishi et al. (2021) proposed a chemical stratification of the environment of the WB789 hot-core, with CH_3OH and all COMs arising from the inner (≤ 0.015 pc) warm (≥ 100 K) region, and SO , CS , H_2CO , $c\text{-C}_3\text{H}_2$, H^{13}CO^+ , and HN^{13}C all associated with an external (≥ 0.05 pc) cold (≤ 40 K) envelope. Our findings also indicate that the species we detect are associated with relatively cold and quiescent envelope material, including CH_3OH . However, the line widths in WB789 are always larger than ~ 2 km s^{-1} even in the envelope tracers, indicating that WB670 and WB789 are different kind of star-forming regions. Simulations show that the abundance of CH_3OH in dense star-forming core is extremely sensitive to dust temperature variations (Acharyya & Herbst 2015; Pauly & Garrod 2018). In particular, the CH_3OH production on grain surfaces depends on the duration of the early cold phase in which CO is hydrogenated on grain mantles, owing to the high volatility of atomic hydrogen (see also Shimonishi et al. 2020).

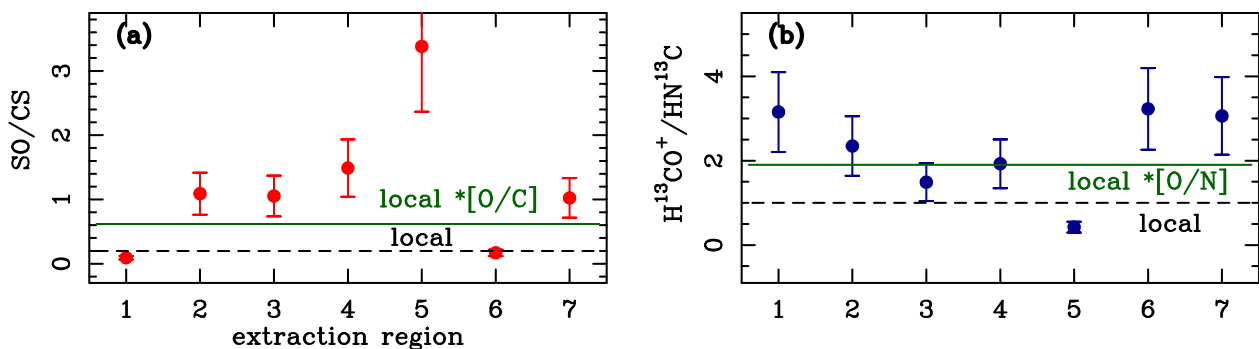


Fig. 8. Column density ratios in the seven molecular extraction regions of WB670. Panel (a) shows the measured SO/CS ratios (points), and compare them to the average SO/CS ratio measured in a sample of inner and local Galaxy high-mass star-forming regions (Fontani et al. 2023, dashed line), and to the expected SO/CS ratio obtained multiplying the local measured value (0.2, dashed line) by the increase in the elemental ratio $[O/C] \sim 3.1$ (horizontal green line) from the Solar circle to $R_{GC} = 23.4$ kpc (Méndez-Delgado et al. 2022). Panel (b) shows the same comparison between the measured $H^{13}CO^+/HN^{13}C$ ratio and the expected ratio obtained multiplying the local measured value for the increase in the $[O/N]$ elemental ratio.

The CH_3OH abundances in N and S are comparable to the so-called organic-poor hot-cores detected in the Large Magellanic Cloud (LMC, Shimonishi et al. 2020; Hamedani Golshan et al. 2024), characterised by values that cannot simply be explained scaling the abundances measured in the local Galaxy for the decreased metallicity (about a factor 2-3, e.g. Andrievsky et al. 2001; Rolleston et al. 2002) of the LMC. Shimonishi et al. (2020) proposed that these organic-poor hot-cores in the LMC could be due to dust temperatures higher than those in organic-rich hot-cores. Therefore, the lower CH_3OH abundance in WB670 could be due to an inefficient (or insufficient) hydrogenation of CO in the stage of ice formation, due to either a (too) warm dust temperature, or to a (too) short cold ice formation stage, or to a (too) low gas density. All scenarios would also predict a lower production efficiency of H_2CO on ice mantles, and this would be in agreement with our finding that H_2CO should be formed in gas phase in WB670. Alternatively, WB670 can be in a late(r) evolutionary stage with respect to WB789, when the molecules in the inner protostellar cocoon(s), including those evaporated from dust grain mantles, have been mostly dissociated by the strong protostellar radiation field. Pauly & Garrod (2018) proposed that CH_3OH abundance could be even enhanced in low-metallicity environments, owing to the lower C/O ratio which would imply that most of C is locked in CO, needed to form CH_3OH . However, this scenario would predict that the CH_3OH abundance in WB670 should be higher than in WB789, because the C/O ratio in WB670 is lower than in WB789 (according to the elemental trends with R_{GC} , see Sect. 1). This is clearly at odds with our observational results. We will better discuss the influence of metallicity on the observed molecular abundances in Sect. 5.4.

5.4. Chemical modelling

To better investigate if the measured column density ratios can constrain the initial elemental abundances, as well as other physical parameters that cannot be derived from the data, we compare our observational results to the prediction of chemical models. We investigate these clouds with the open-source gas-grain chemistry code UCLCHEM (Holdship et al. 2017). This time-dependent astrochemical code allows us to model the evolution of each molecule. We considered a "static model", namely an isothermal cloud at constant density with a radius of $R = 0.5$ pc (the maximum radius of the modelled regions), and we explored

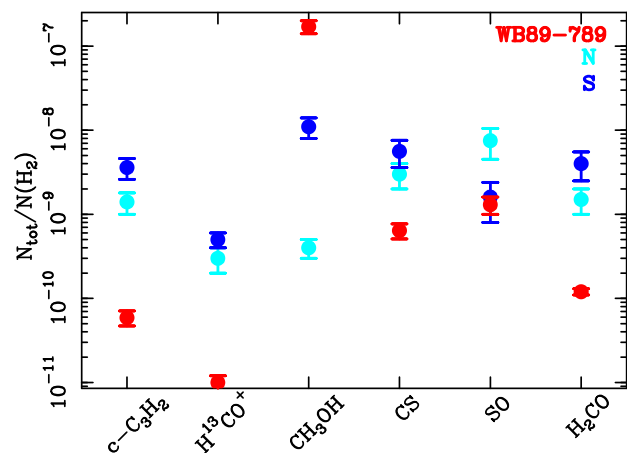


Fig. 9. Fractional abundances with respect to H_2 derived for N, S, and WB789. The WB789 abundances were derived on a hot-core linear size of 0.1 pc (Shimonishi et al. 2021).

a range of physical and chemical conditions. The parameters include H_2 number density (cm^{-3}), gas temperature, cosmic-ray ionisation rate ζ , radiation field F_{UV} , and both the initial oxygen and carbon abundances as listed in Table 6. Each of the models is ran with an edge visual extinction of $A_v = 1.0$ mag, and molecular ratios are computed at 10^6 years. The grid is discussed in more detail in Vermariën et al. (in prep.). We converted between $^{12}C/^{13}C$ using a conversion factor of $10^{1.8}$ (~ 68) since the chemical network did not include isotopologues. For the modelling, we used a conventional gas-to-dust mass ratio of 100. We discuss the details of using the observed value obtained from Giannetti et al. (2017) at the end of this section.

We excluded models for which the predicted fractional abundances of our molecules is below 10^{-13} . This results in a total of 710 models out of the original 65536. These models can then be compared to the observations, and the distributions of the fit of the theoretical ratios with the observed ones are shown in Fig. 10, sorted in descending averaged mean squared error between the models and observations. Some ratios, namely CS/HCO^+ , CS/SO , HCO^+/H_2CO , HCO^+/HCS^+ , SO/H_2CO , SO/HCS^+ , CS/HCO , HCO/H_2CO and CS/HNC , have no overlap between the models and the observations. Some observed ratios also lie in the tails of the model distribution. Overall, it is very unlikely to find a model that fits all ratios well.

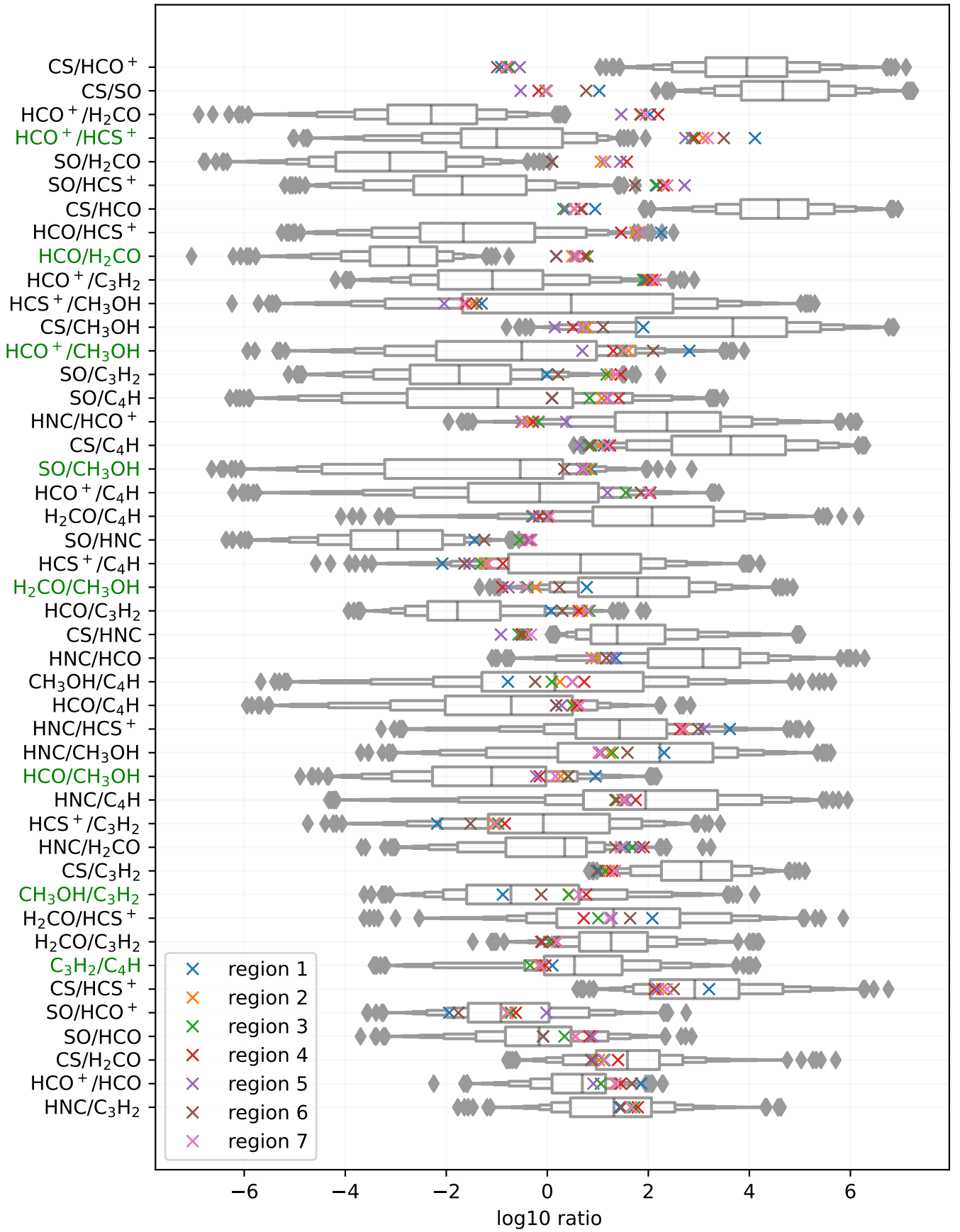


Fig. 10. A comparison of the distribution of log-ratios of the observed species, with the ratios shown in Fig. 6 highlighted in green. The seven observed region's ratios (coloured markers) are plotted against the distribution of the modelled ratios (grey boxen plots). The molecules are sorted from top to bottom in order of decreasing error.

Parameter	Min	Max	Sample space
Density n_{H} (cm^{-3})	1×10^3	1×10^7	log
Temperature T (K)	10	100	linear
Cosmic-ray ionisation rate ζ (s^{-1})	1×10^{-17}	1×10^{-14}	log
Radiation field F_{UV} (Habing)	0.1	100	log
Initial elemental abundance of oxygen $f_{\text{O}}/f_{\text{O},\odot}$	$0.05 \times 3.34 \times 10^{-4}$	$1.0 \times 3.34 \times 10^{-4}$	linear
Initial elemental abundance of carbon $f_{\text{C}}/f_{\text{C},\odot}$	$0.05 \times 1.77 \times 10^{-4}$	$1.0 \times 1.77 \times 10^{-4}$	linear

Table 6. Ranges of physical and chemical parameters of the grid of models.

In order to further constrain the physical parameter space, the 50 models with the lowest Mean Squared Error (MSE) are chosen. Figure 11 shows again the comparison between the models and the observations. The distribution of the models is now closer to the observations, so the horizontal axis is more compact than in Fig. 10. Many of the ratios distance between models and observations decrease considerably by taking only the best models, but the CS, HCS⁺ and H₂CO based ratios do not improve.

In addition to the ratios that could not be explained by just the “observable” ratios, some ratios also have no matching distribution with the subset of best models. It does show however that we can fit many of the ratios well with the subset of best models. By plotting the error for each of the ratios in a pairwise grid, as can be seen in Fig. 12, we can better understand which molecules have the lowest error. This shows the molecules were best fit in the following order: *c*-C₃H₂, HNC, HCO, C₄H, CH₃OH, HCO⁺, SO, H₂CO, HCS⁺, and finally CS. We then plot the distribution of the physical and chemical parameters investigated in the grid (Fig. 13). The models indicate densities ranging from 10^3 to $10^{3.6}$ cm^{-3} , temperatures from 20 to 45 K, radiation fields lower than 5 Habing, and cosmic-ray ionisation rate ζ in a wide range from the interstellar value of $\sim 10^{-17}$ s^{-1} up to $\sim 10^{-14}$ s^{-1} . Oxygen and carbon initial abundances both larger than 1/5th of the Solar value are favoured by the models. Additionally, the [O/C] ratio favours values in between ~ 2 and 5, with a small distribution of even higher oxygen enhancements. The densities measured in N and S are higher ($\sim 10^4$ cm^{-3}) than the values predicted by the models, which, however, refer to the molecular regions, all more extended than N and S. Moreover, assuming β as in Table 3 to compute $N(\text{H}_2)$, we derive densities of the order of $\sim 10^3$ cm^{-3} , consistent with model predictions.

Lastly we investigate the time-dependence of these ratios (Fig. 14) in order to gauge whether the observed star-forming regions exhibit a younger or older chemical history. Figure 14 shows that for most molecules the fits would not improve at another time, apart from the H₂O/CH₃OH, CS/HNC and CS/SO ratios who might benefit from sampling at a later time. However this would make the fits for other ratios worse. For some molecules there seems to be no time at which the ratios are fit correctly. The worst performing molecule, CS, clearly shows an over-prediction in the model as compared to the observations. However, such inconsistency can be due to a neglected high optical depth in the derivation of the observed column densities.

Overall, our results indicate that static models as those investigated here can give a range of physical parameters that best match with the observations, but are not optimal to reproduce the set of observed abundances. A more proper fit for each region would need dynamical modelling, accounting for collapse during the time dependent evolution. The range of values predicted from the static models suggest that low energetic conditions, in particular low temperatures (20–45 K) and F_{UV} lower than 5 Habing, are favoured, consistent with the location of the source in the Galactic anti-Centre (certainly more “quiescent”

than the local and inner Galaxy). The models also predict that the oxygen elemental abundance should not be smaller than 1/5th of the Solar value, consistent with an extrapolation of the Méndez-Delgado et al. (2022) trend which predicts a decrease of a factor 4.6. The carbon elemental abundance should also not be smaller than $\sim 1/5$ th of the Solar value, but this is well above the value extrapolated from the Méndez-Delgado et al. (2022) trend at 23.4 kpc, that is $\sim 1/14$ th of the Solar value. If confirmed by models that include dynamical collapse, such difference would indicate a [C/H] gradient that flattens in the far-outer Galaxy with respect to the trend derived at inner R_{GC} . Indeed, elemental Galactocentric gradients derived from observations of HII regions in spiral galaxies characterised by extended H I envelopes indicate a flattening of the radial distribution of metals at large galactocentric distances (Bresolin 2017). An elemental gradient of carbon flatter than expected in the OG would also explain why the abundance trends with R_{GC} of organics tend to be less steep than the extrapolated gradients (Bernal et al. 2021; Fontani et al. 2022b).

Another caveat arises from the assumed gas-to-dust mass ratio, which could be higher than that assumed (100) according to the trend proposed by Giannetti et al. (2017) ($\sim 3000^{+700}_{-2200}$). We thus performed two tests, one for a model at low density ($\sim 10^3$ cm^{-3}) and one at high density ($\sim 10^6$ cm^{-3}). In the low density case, the results do not show any significant differences. In the high density case, some differences are found, but this case does not represent WB670. Moreover, no firm measurements of this ratio are so far obtained, to our knowledge, at such large R_{GC} , and hence assuming a gas-to-dust ratio significantly different from the standard one will introduce a further uncertainty in the models.

6. Conclusions

We used ALMA to observe WB670, the source with the largest Galactocentric distance (23.4 kpc) in CHEMOUT, at a resolution of ~ 15000 au. We detected emission of *c*-C₃H₂, C₄H, CH₃OH, H₂CO, HCO, H¹³CO⁺, HCS⁺, CS, HN¹³C, and SO, derived their column densities, and compared the observational results with chemical model predictions. The main results of our study are the following:

- The molecular emission arises from a filamentary structure oriented SE-NW, where multiple cores are detected. The filament seems more extended than the ALMA primary beam. The morphology is different in each tracer. The most intense emission of molecular ions, carbon-chain molecules, and H₂CO is associated with two millimeter continuum, infrared-bright cores. On the contrary, the CH₃OH and SO most intense emission arises predominantly from the part of the filament with no continuum sources. The narrow linewidths ($\sim 1 - 2$ km s^{-1}) across the filament indicate quiescent gas, despite the presence of the infrared-bright sources;

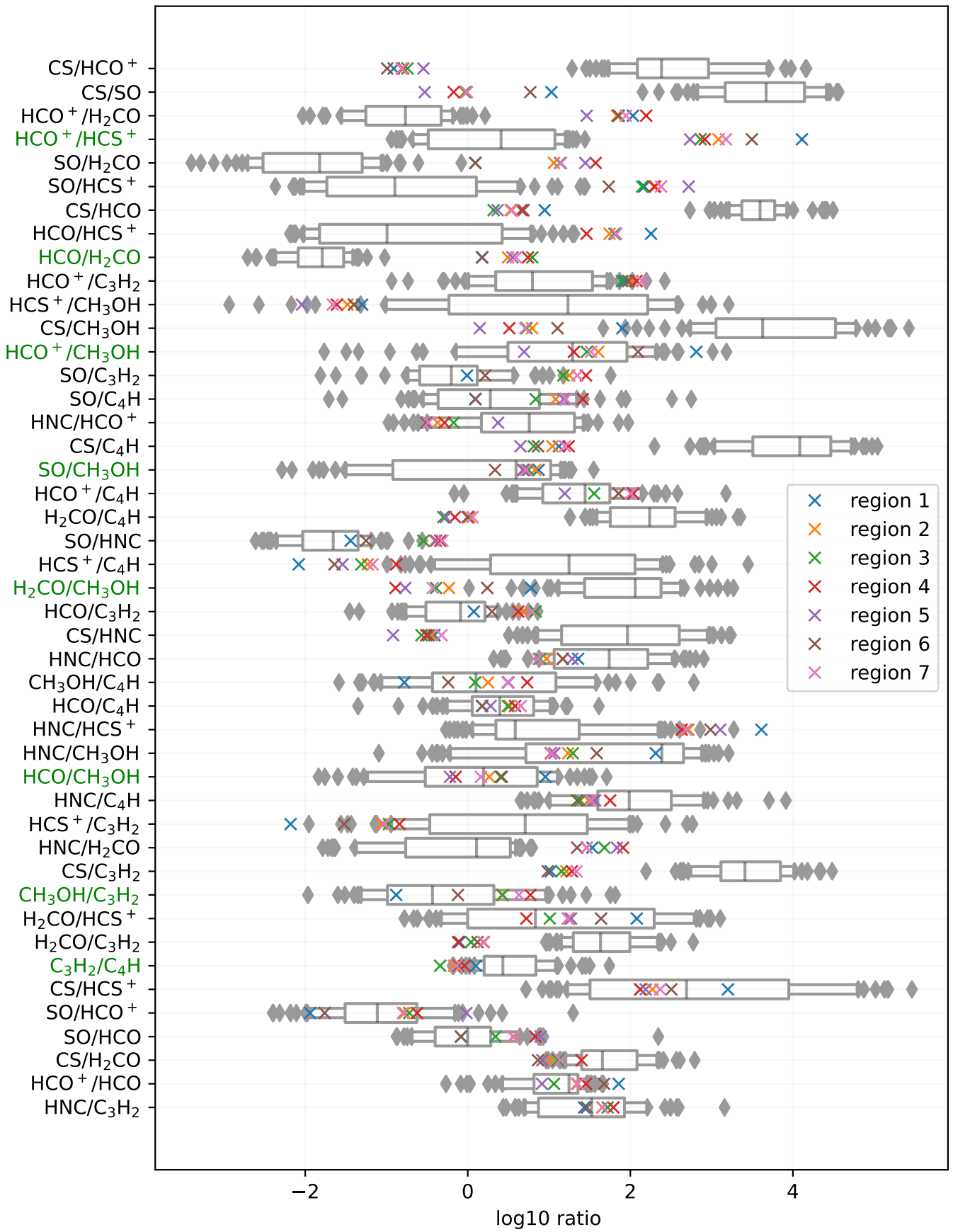


Fig. 11. The best 50 best models (grey boxen plots) compared to the 7 observed regions (coloured markers).

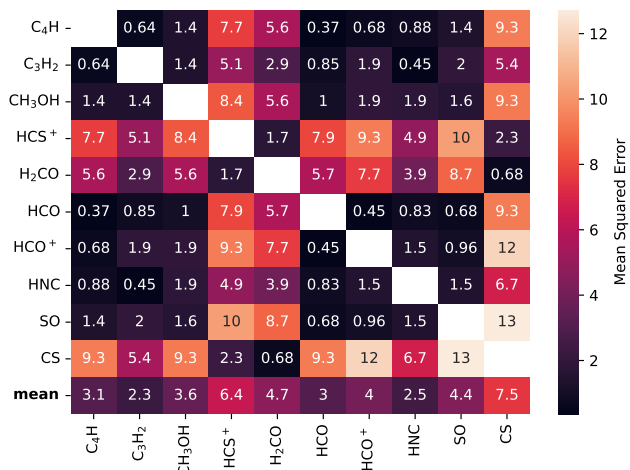


Fig. 12. The mean squared error (MSE) computed between all of the regions and the best 50 models. The averaged MSE for each molecule is included on the bottom row.

- From a LTE analysis of the CH₃OH lines, their excitation temperatures are quite low (7–15 K) and could be under-thermally excited. Derived molecular column densities are comparable with those in local star-forming regions. There seems to be a spatial anti-correlation between the column density of hydrocarbons, molecular ions, HCO, and H₂CO on one side, and CH₃OH and SO on the other. This would possibly suggest different formation processes for the two groups of molecules (gas phase processes versus surface processes);
- CH₃OH fractional abundances calculated towards the millimeter continuum cores ($0.4 - 11 \times 10^{-9}$) are consistent with those of the so-called organic-poor cores found in the LMC, where such low CH₃OH abundances could be due to an inefficient hydrogenation of CO on grain mantles;
- Static models that best match the observed column densities favour diffuse gas and low irradiation conditions (expected at large Galactocentric radii), but carbon elemental abundances 3 times higher than that derived extrapolating the [C/H] elemental Galactocentric gradient at 23 kpc. This would indicate a flatter [C/H] trend at large Galactocentric radii, in line with a flat abundance of organics. Models including dynamical evolution should be able to more properly reproduce the chemical composition of WB670.

The results of this work indicate that a proper comparison between observations and models starting from a huge grid of parameters is essential to properly model the chemistry. Our study would greatly benefit from new observations of more molecular species and more lines at the same (at least) spatial resolution as that obtained here. In particular, tracers of the cosmic-ray ionisation rate, basically unconstrained by our study, would be particularly relevant.

Acknowledgements. This paper makes use of the following ALMA data: ADS/JAO.ALMA#2022.1.00911.S. ALMA is a partnership of ESO (representing its member states), NSF (USA) and NINS (Japan), together with NRC (Canada), MOST and ASIAA (Taiwan), and KASI (Republic of Korea), in cooperation with the Republic of Chile. The Joint ALMA Observatory is operated by ESO, AUI/NRAO and NAOJ. F.F., S.V., G.V., and D.G. acknowledge support from the European Research Council (ERC) Advanced grant MOPPEX 833460. L.C. and V.M.R. acknowledges support from the grant PID2022-136814NB-I00 by the Spanish Ministry of Science, Innovation and Universities/State Agency of Research MICIU/AEI/10.13039/501100011033 and by ERDF, UE; V.M.R.

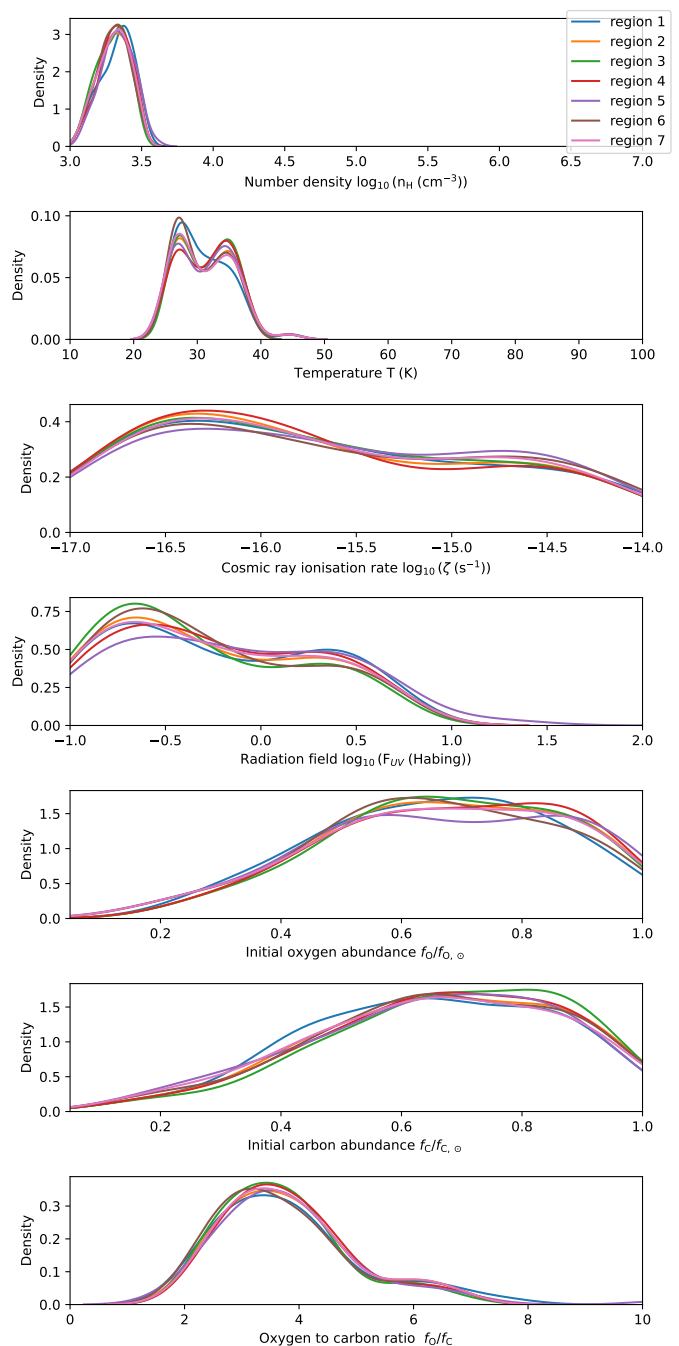


Fig. 13. A kernel density probability estimate of the physical parameters for the best 50 models, fit separately for each of the regions, indicated by the coloured curves as labelled in the top-right.

also acknowledge support from the grant RYC2020-029387-I funded by MICIU/AEI/10.13039/501100011033 and by "ESF, Investing in your future", and from the Consejo Superior de Investigaciones Científicas (CSIC) and the Centro de Astrobiología (CAB) through the project 20225AT015 (Proyectos intramurales especiales del CSIC); and from the grant CNS2023-144464 funded by MICIU/AEI/10.13039/501100011033 and by "European Union NextGenerationEU/PRTR". A.S.-M. acknowledges support from the RYC2021-032892-I grant funded by MCIN/AEI/10.13039/501100011033 and by the European Union "Next GenerationEU"/PRTR, as well as the program Unidad de Excelencia María de Maeztu CEX2020-001058-M, and support from the PID2020-117710GB-I00 (MCI-AEI-FEDER, UE).

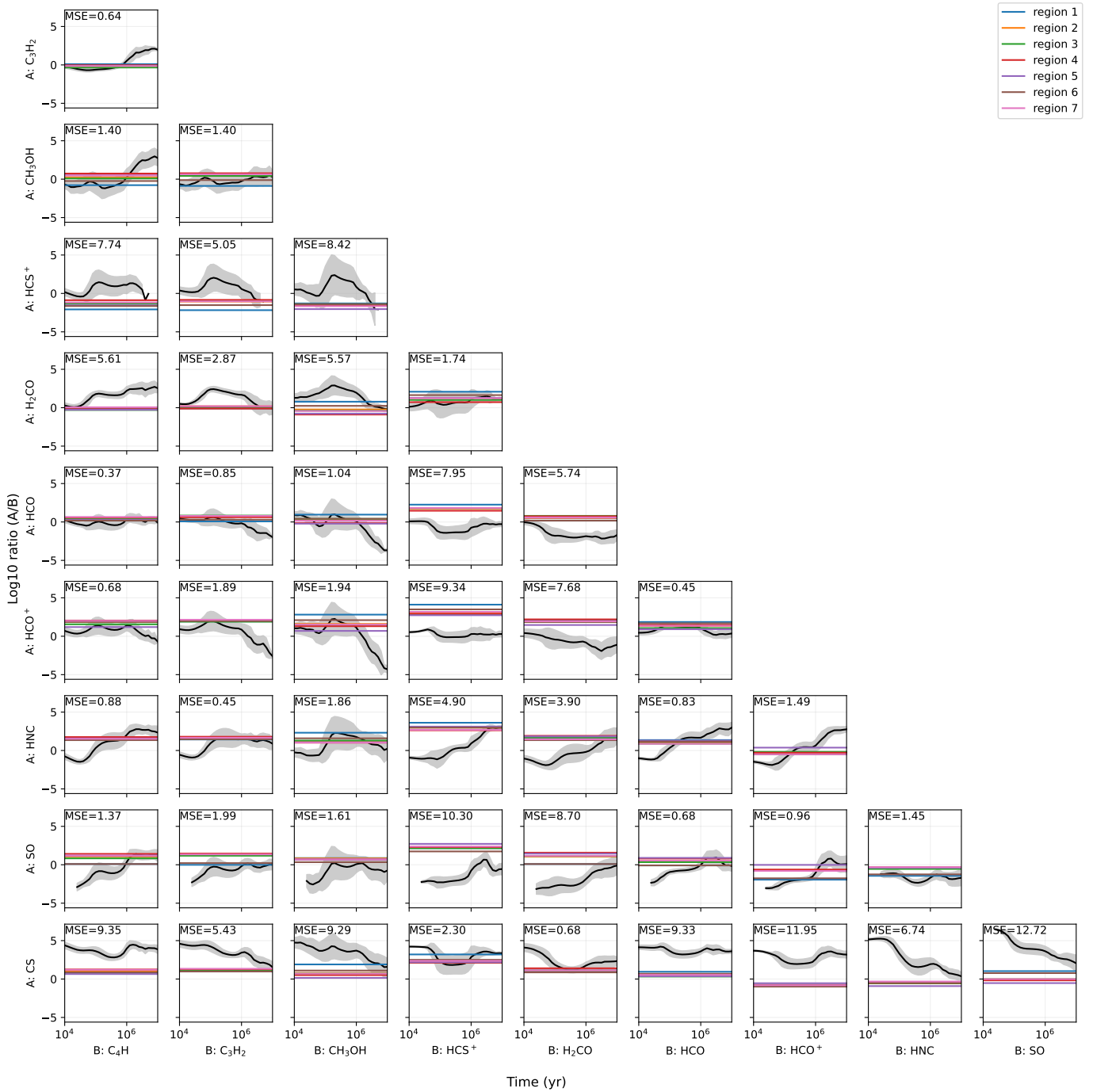


Fig. 14. The evolution of the observable ratios as a function of time for the best 50 models, with the mean squared error at 10⁶ years.

References

- Acharyya, K. & Herbst, E. 2015, *ApJ*, 812, 142A
 Andrievsky, S.M., Kovtyukh, V.V., Korotin, S.A., et al. 2001, *A&A*, 367, 605
 Arellano-Córdova, K.Z., Esteban, C., García-Rojas, J., Méndez-Delgado, J.E. 2020, *MNRAS*, 496, 1051
 Barnes, A.T., Lui, J., Zhang, Q., et al. 2023, *A&A*, 675, 53
 Battersby, C., Ginsburg, A., Bally, J., et al. 2014, *ApJ*, 787, 113
 Bernal, J.J., Sephus, C.D., Ziurys, L.M. 2021, *ApJ*, 922, 106
 Blair, S.K., Magnani, L., Brand, J., Wouterloot, J.G.A. 2008, *AsBio*, 8, 59
 Bresolin, F. 2017, *ASSL*, 434, 145
 Buchhave, L.A., Latham, D.W., Johansen, A., Bizzarro, M., Torres, G., et al. 2012, *Nature*, 486, 375
 Cacciapuoti, L., Testi, L., Podio, L., et al. 2024, *ApJ*, 961, 90
 Chacón-Tanarro, A., Caselli, P., Bizzocchi, L., Pineda, J.E., Sipilä, O., et al. 2019a, *A&A*, 622, 141
 Chacón-Tanarro, A., Pineda, J.E., Caselli, P., et al. 2019b, *A&A*, 623, 118

- Colzi, L., Romano, D., Fontani, F., et al. 2022, *A&A*, 667, A151
 Cutri, R.M. et al., 2003, The IRSA 2MASS All-Sky Point Source Catalogue, NASA/IPAC Infrared Science Archive. Available at: <http://irsa.ipac.caltech.edu/applications/Gator/>
 Draine, B.T., & Lee, H.M. 1984, *ApJ*, 285, 89
 Endres, P., Schlemmer, S., Schilke, P., Stutzki, J., Müller, H.S.P. 2016, *J.Mol.Spec.*, 327, 95
 Esteban, C., Fang, X., García-Rojas, J., Toribio San Cipriano, L. 2017, *MNRAS*, 471, 987
 Fontani, F., Cesaroni, R., Caselli, P., Olmi, L. 2002, *A&A*, 389, 603
 Fontani, F., Busquet, G., Palau, Aina, et al. 2015, *A&A*, 575, A87
 Fontani, F., Barnes, A.T., Caselli, P., et al. 2021, *MNRAS*, 503, 4320
 Fontani, F., Colzi, L., Bizzocchi, L., Rivilla, V.M., Elia, D. et al. 2022, *A&A*, 660, A76
 Fontani, F., Schmiedeke, A., Sánchez-Monge, Á., et al. 2022b, *A&A*, 664, A154
 Fontani, F., Roueff, E., Colzi, L., Caselli, P. 2023, *A&A*, 680, A58

- Forbrich, J., Lada, C.J., Lombardi, M., et al. 2015, *A&A*, 580, 114
- Freeman, P., Bottinelli, S., Plume, R., et al. 2023, *A&A*, 678, 18
- Friesen, R.K., Pon, A., Bourke, T.L., et al. 2018, *ApJ*, 869, 158
- Fuchs, G. W., Cuppen, H. M., Ioppolo, S., et al. 2009, *A&A*, 505, 629
- Galametz, M., Maury, A.J., Valdivia, V., et al. 2019, *A&A*, 632, 5
- Garrod, R., Park, I.H., Caselli, P., Herbst, E. 2006, *FaDi*, 133 51
- Giannetti, A., Leurini, S., König, S., et al. 2017, *A&A*, 606, L12
- Gonzalez, G., Brownlee, D., Ward, P. 2001, *Icarus*, 152, 185
- Hamedani Golshan, R., Sánchez-Monge, Á., Schilke, P., et al. 2024, arXiv:2405.01710
- Holdship, J., Viti, S., Jiménez-Serra, I., et al. 2017, *AJ*, 154, 38
- Higuchi, A. E., Sakai, N., Watanabe, Y., et al. 2018, *ApJS*, 236, 52
- Jensen, S.S., Spezzano, S., Caselli, P., Grassi, T., Haugbølle, T. 2023, *A&A*, 675, A34
- Kauffmann, J., Bertoldi, F., Bourke, T.L., et al. 2008, *A&A*, 487, 993
- Kong, S., Tan, J.C., Caselli, P., et al. 2017, *ApJ*, 834, 193
- Maliuk, A. & Budaj, J. 2020, *A&A*, 635, 191
- Martín, S., Martín-Pintado, J., Blanco-Sánchez, C., Rivilla, V.M., Rodríguez-Franco, A., Rico-Villas, F. 2019, *A&A*, 631, 159
- Méndez-Delgado, J.E., Amayo, A., Arellano-Córdova, K.Z., Esteban, C., García-Rojas, J., Carigi, L., Delgado-Inglada, G. 2022, *MNRAS*, 510, 4436
- Milam, S.N., Savage, C., Brewster, M.A., Ziurys, L.M. 2005, *ApJ*, 634, 1126
- Ossenkopf, V. & Henning, Th. 1994, *A&A*, 291, 943
- Pauly, T. & Garrod, R.T. 2018, *ApJ*, 854, 13
- Pickett, H.M., Poynter, R.L., Cohen, E.A., et al. 1998, *J. Quant. Spectr. Rad. Transf.*, 60, 883
- Ramírez, I., Asplund, M., Baumann, P., Meléndez, J., Bensby, T. 2010, *A&A*, 521, A33
- Ramal-Olmedo, J.C., Menor-Salván, C.A., Fortenberry, R.C. 2021, *A&A*, 656, A148
- Rivilla, V.M., Beltrán, M.T., Vasyunin, A., Caselli, P., Viti, S., Fontani, F., Cesaroni, R. 2019, *MNRAS*, 483, 806
- Rolleston, W.R.J., Trundle, C., Dufton, P. L. 2002, *A&A*, 396, 53
- Romano, D., Franchini, M., Grisoni, V., Spitoni, E., Matteucci, F., Morossi, C. 2020, *A&A*, 639, 37
- Sánchez-Monge, Á, Palau, Aina, Fontani, F., et al. 2013, *MNRAS*, 432, 3288
- Sewiło, M., Indebetouw, R., Charnley, S.B., Zahorecz, S., Oliveira, J.M. et al. 2018, *ApJL*, 853, L19
- Shimonishi, T., Watanabe, Y., Nishimura, Y., Aikawa, Y., Yamamoto, S., et al. 2018, *ApJ*, 891, 164
- Shimonishi, T., Das, A., Sakai, N., et al. 2020, *ApJ*, 891, 164
- Shimonishi, T., Izumi, N., Furuya, K., Yasui, C. 2021, *ApJ*, 922, 206
- Silsbee, K., Akimkin, V., Ivlev, A.V., et al. 2022, *ApJ*, 940, 188
- Sipilä, O., Spezzano, S., Caselli, P. 2016, *A&A*, 591, L1
- Spezzano, S., Bizzocchi, L., Caselli, et al. 2016, *A&A*, 592, L11
- Testi, L., Birnstiel, T., Ricci, L., et al. 2014, *Protostars and Planets VI*, Henrik Beuther, Ralf S. Klessen, Cornelis P. Dullemond, and Thomas Henning (eds.), University of Arizona Press, Tucson, 339
- Vasyunina, T., Linz, H., Henning, Th., et al. 2011, *A&A*, 527, 88
- Vidal, T.H.G., Loison, J.-C., Jaziri, A.Y. et al. 2017, *MNRAS*, 469, 435
- Ysard, N., Koehler, M., Jiménez-Serra, I., et al. 2019, *A&A*, 631, A88
- Wouterloot, J.G.A. & Brand, J. 1989, *A&AS*, 80, 149
- Wright, E.L., et al. 2010, *AJ*, 140, 1868
- Zinchenko, I., Caselli, P., Pirogov, L. 2009, *MNRAS*, 395, 2234

Appendix A: Maps

The maps of the integrated emission in Fig. 4 are shown, enlarged, in Figures A.1–A.6.

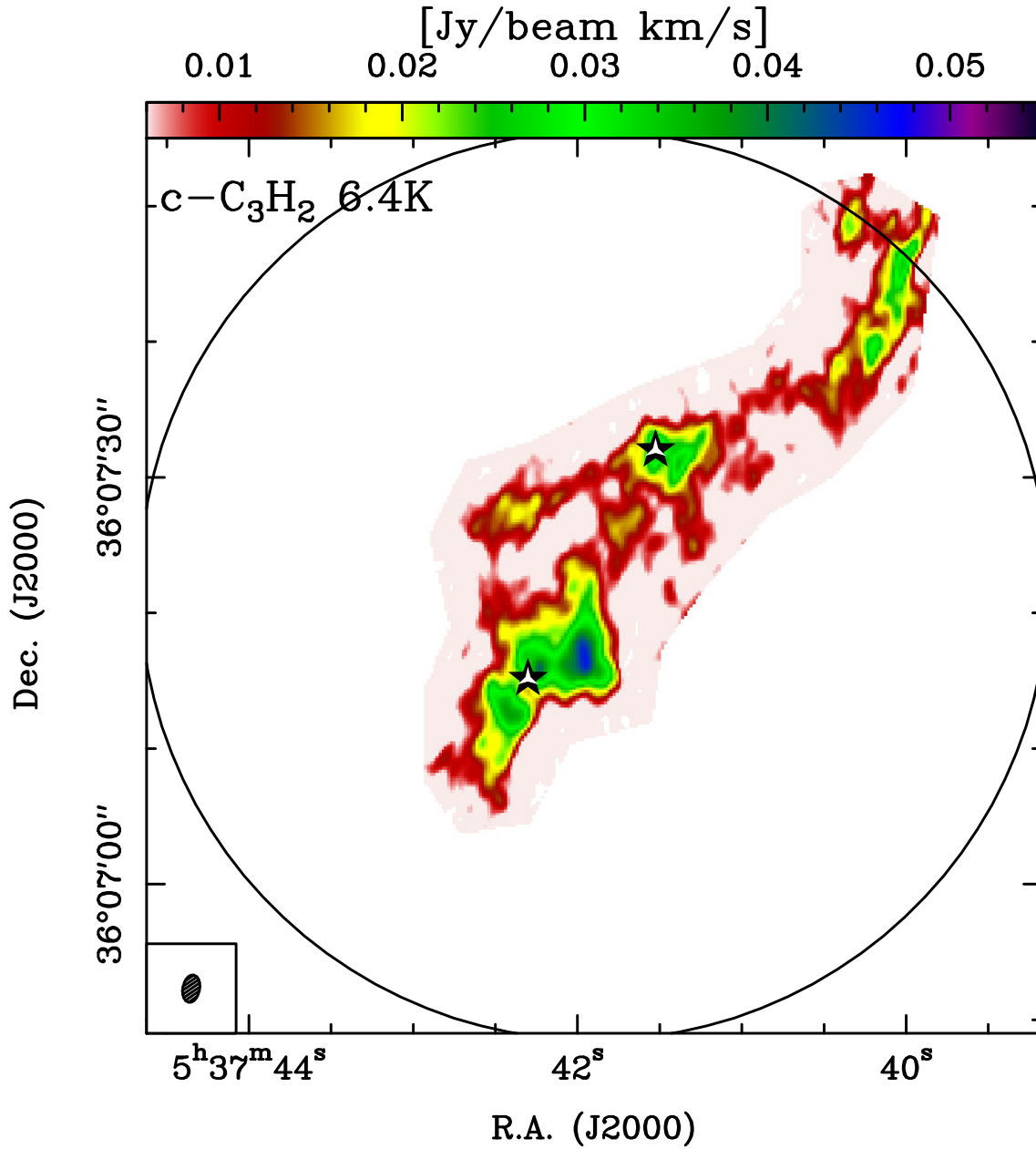


Fig. A.1. Velocity-integrated emission map of $c\text{-C}_3\text{H}_2$ $J(K_a, K_b) = 2(1, 2) - 1(0, 1)$. The map is the same shown in Fig. 4, so we refer to that figure caption for details.

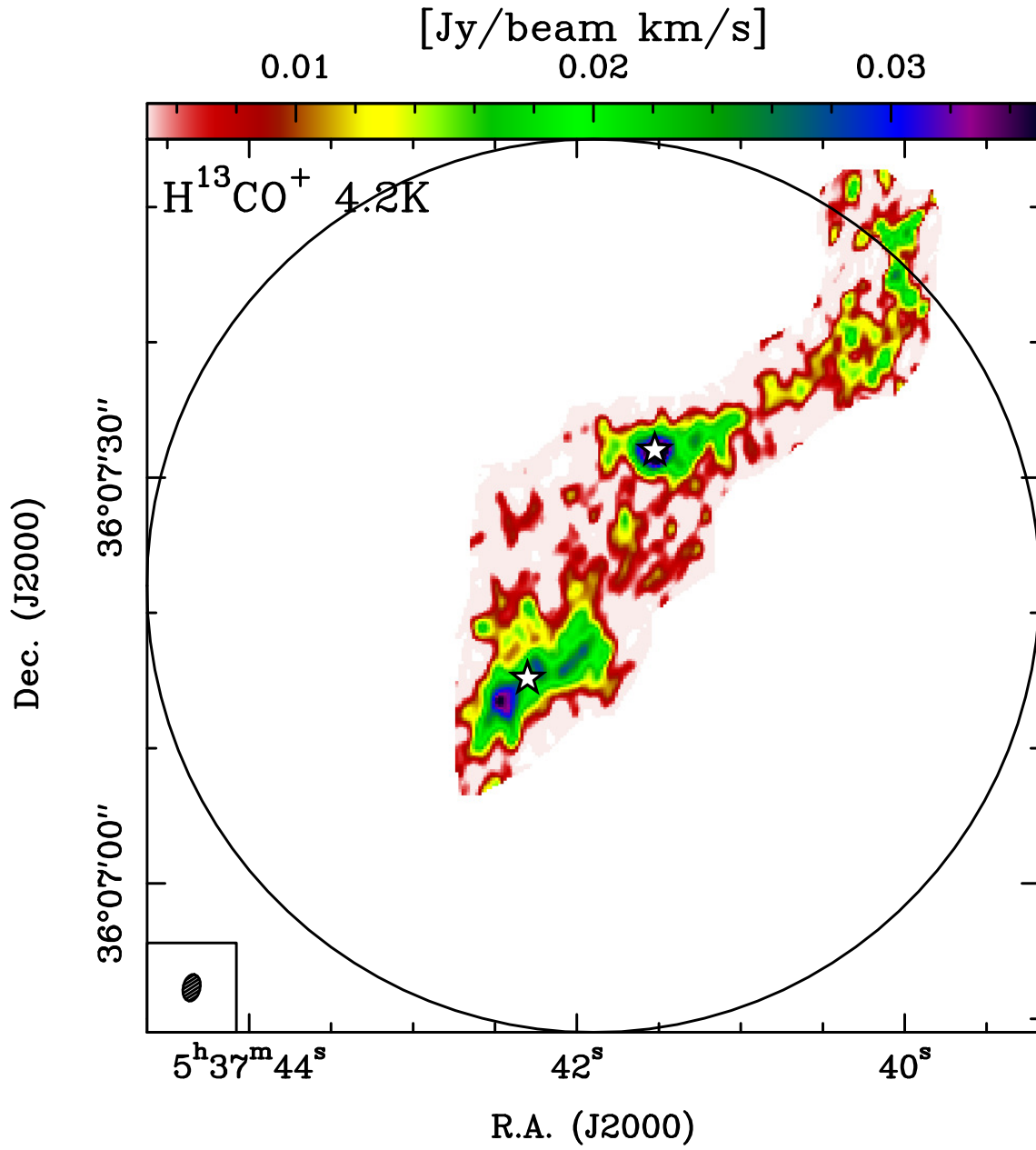


Fig. A.2. Same as Fig. A.1 for H^{13}CO^+ $J = 1 - 0$.

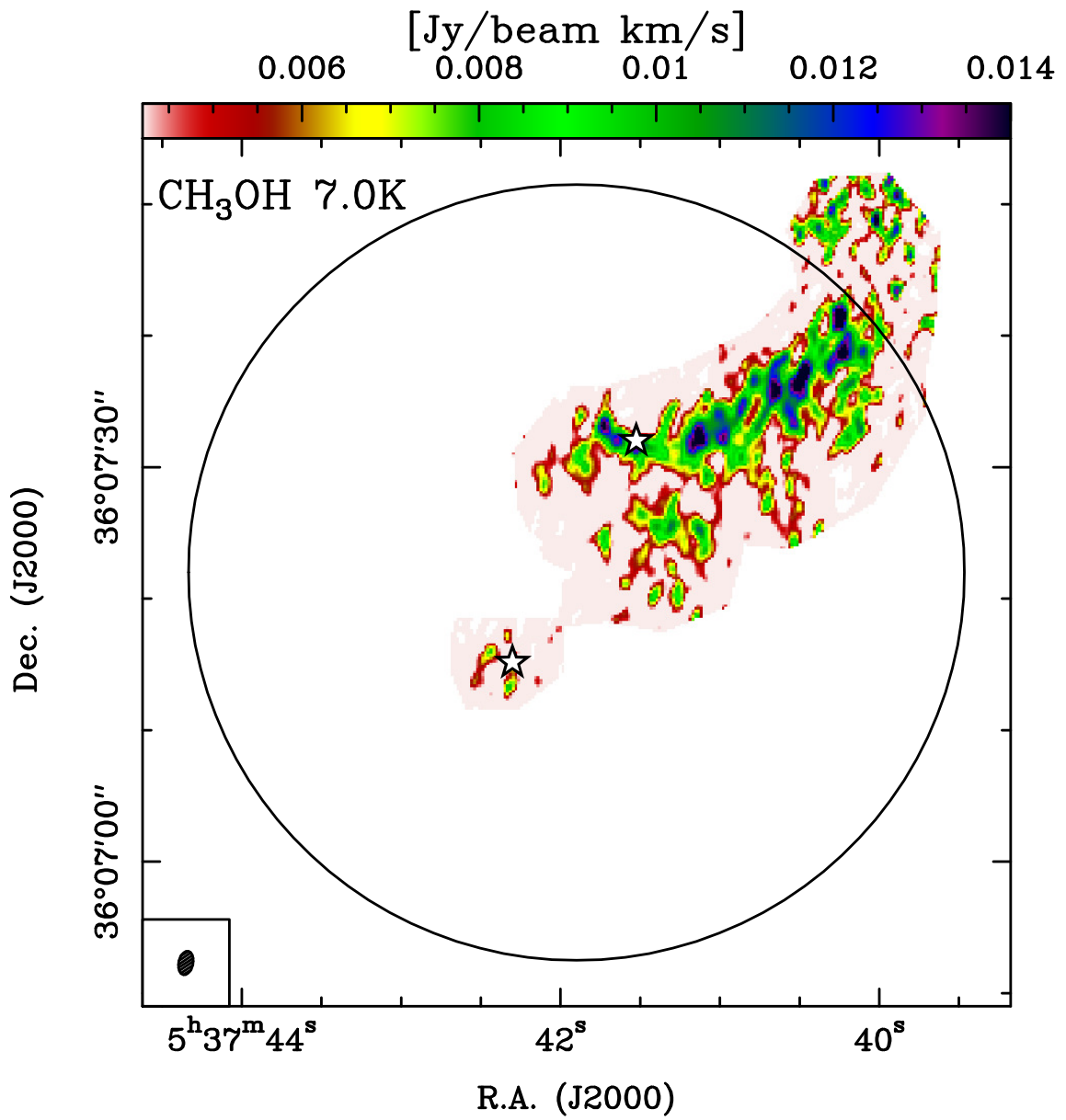


Fig. A.3. Same as Fig. A.1 for CH₃OH $J(K_a, K_b) = 2(0, 1) - 1(0, 1)A^+$.

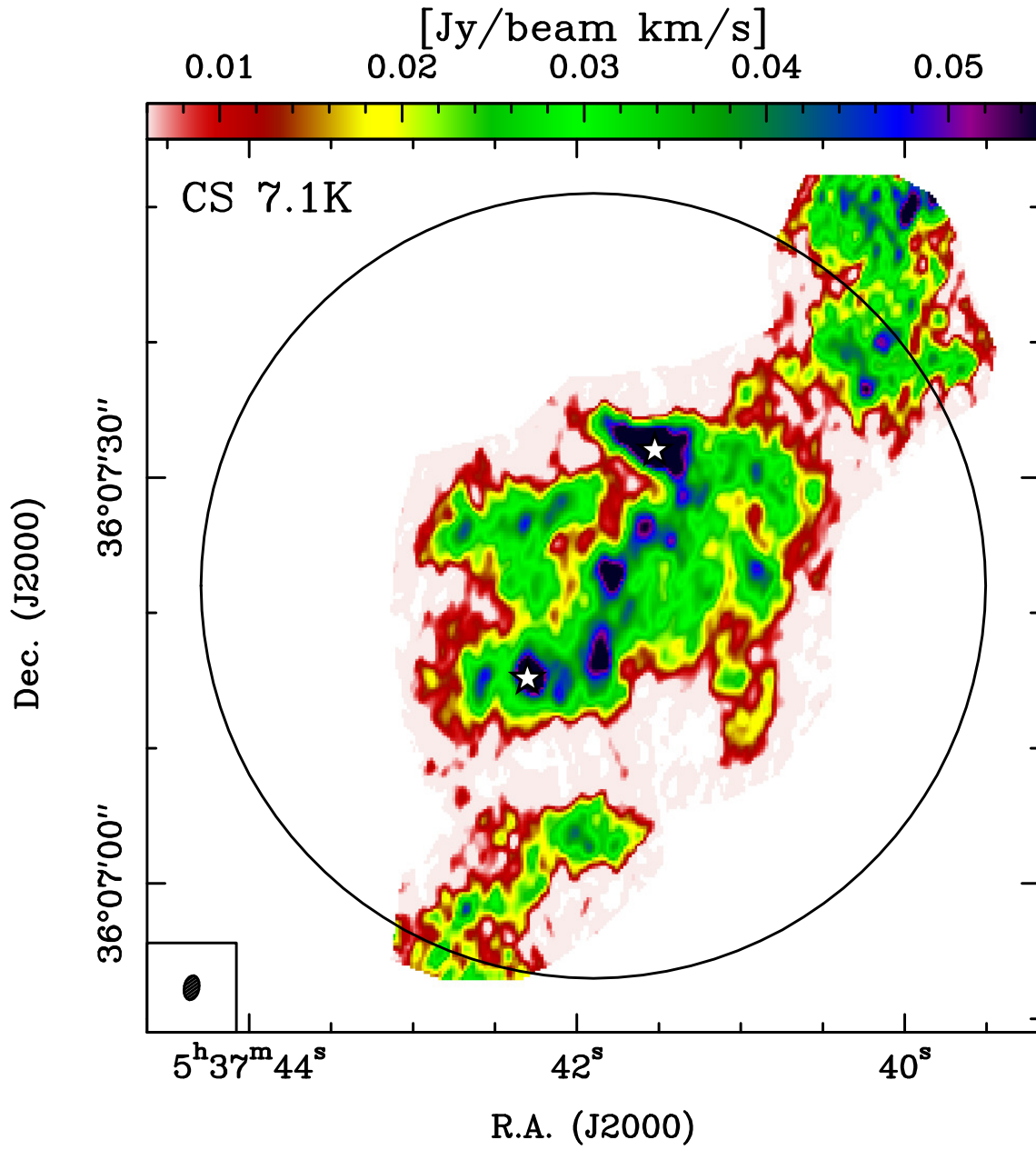


Fig. A.4. Same as Fig. A.1 for CS $J = 2 - 1$.

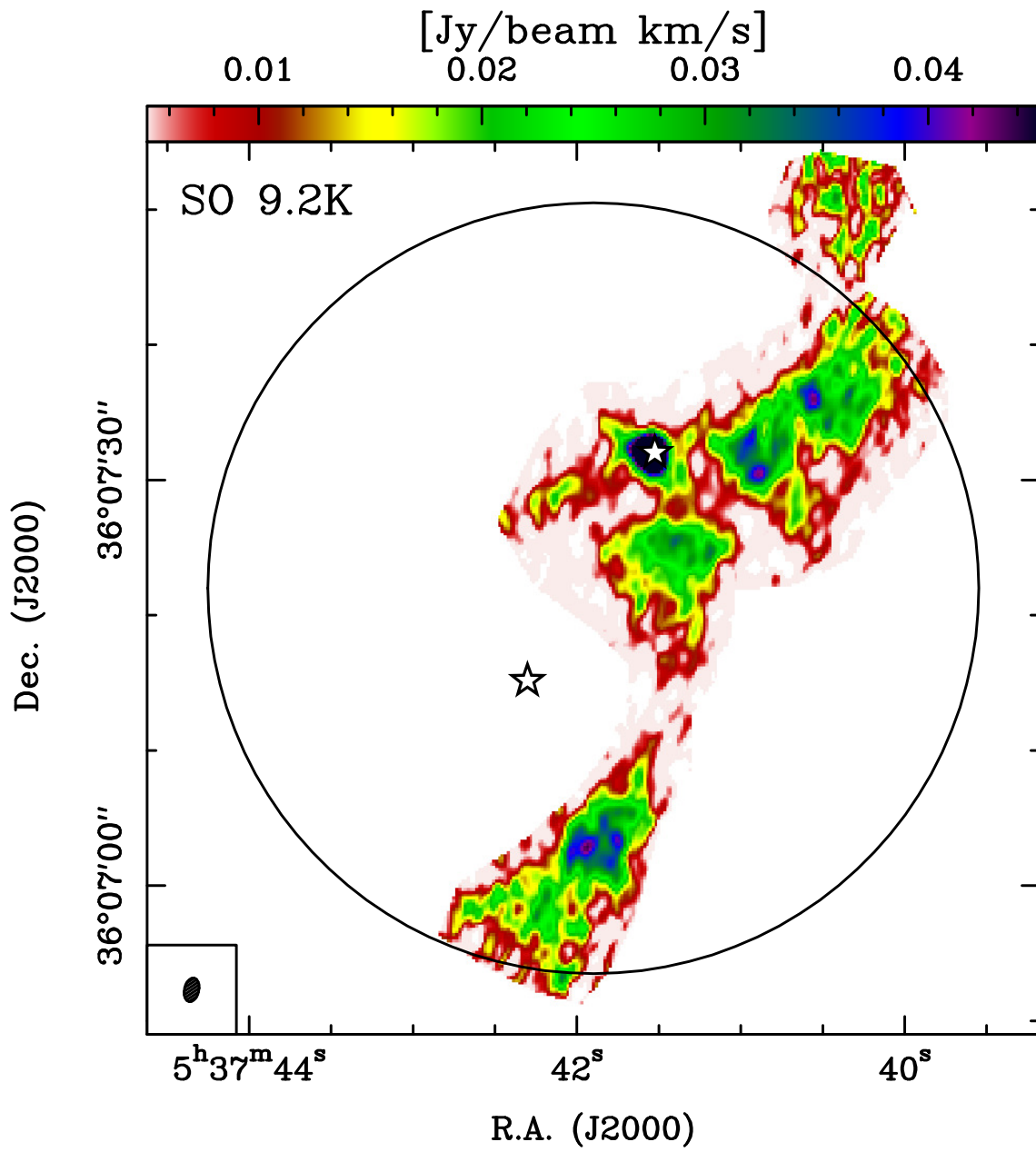


Fig. A.5. Same as Fig. A.1 for SO $J(K) = 3(2) - 2(1)$.

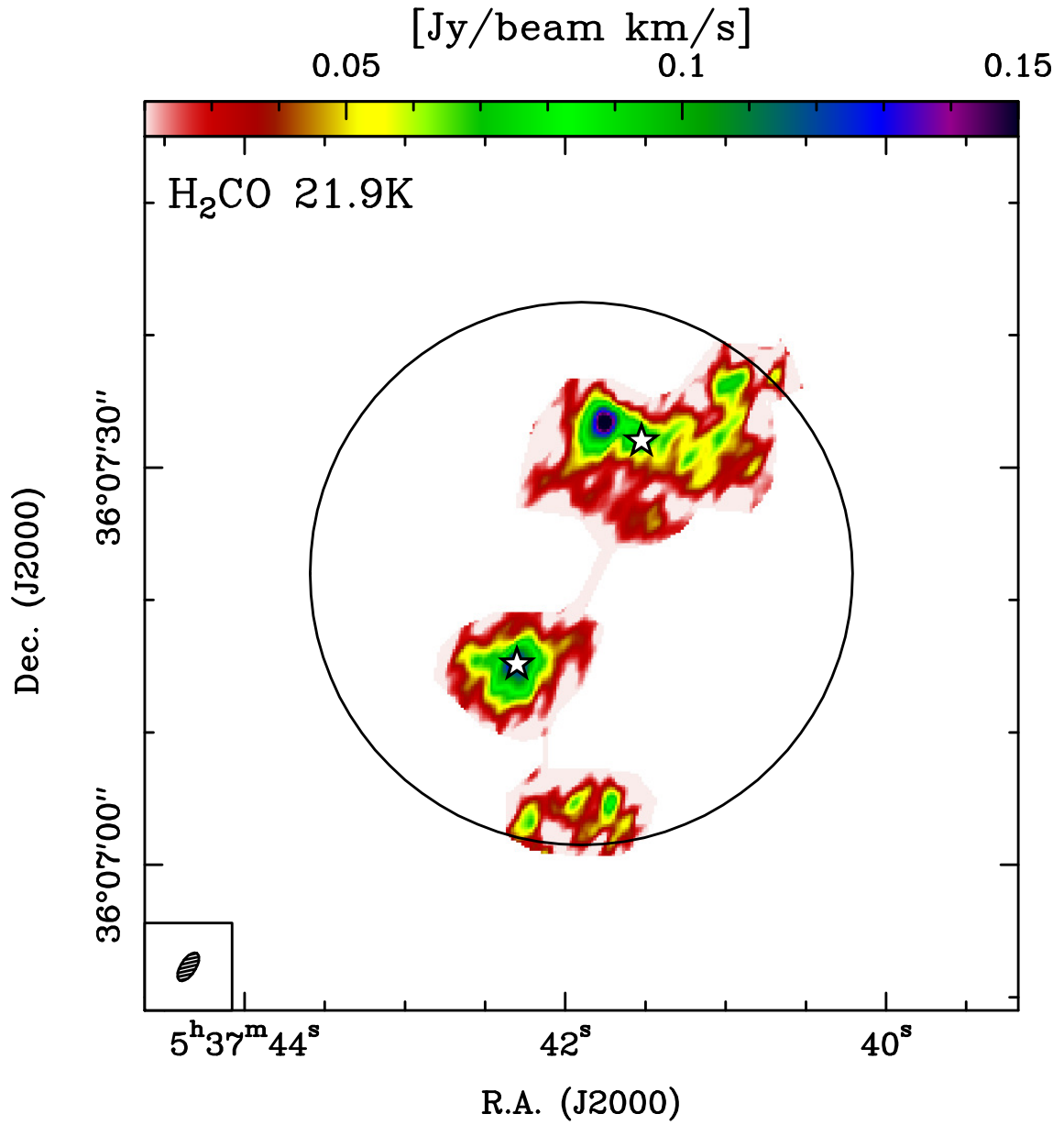


Fig. A.6. Same as Fig. A.1 for H₂CO $J(K_a, K_b) = 2(1, 2) - 1(1, 1)$.

Appendix B: Spectra

Spectra of the detected lines, extracted from the regions identified in Sect. 3.3.

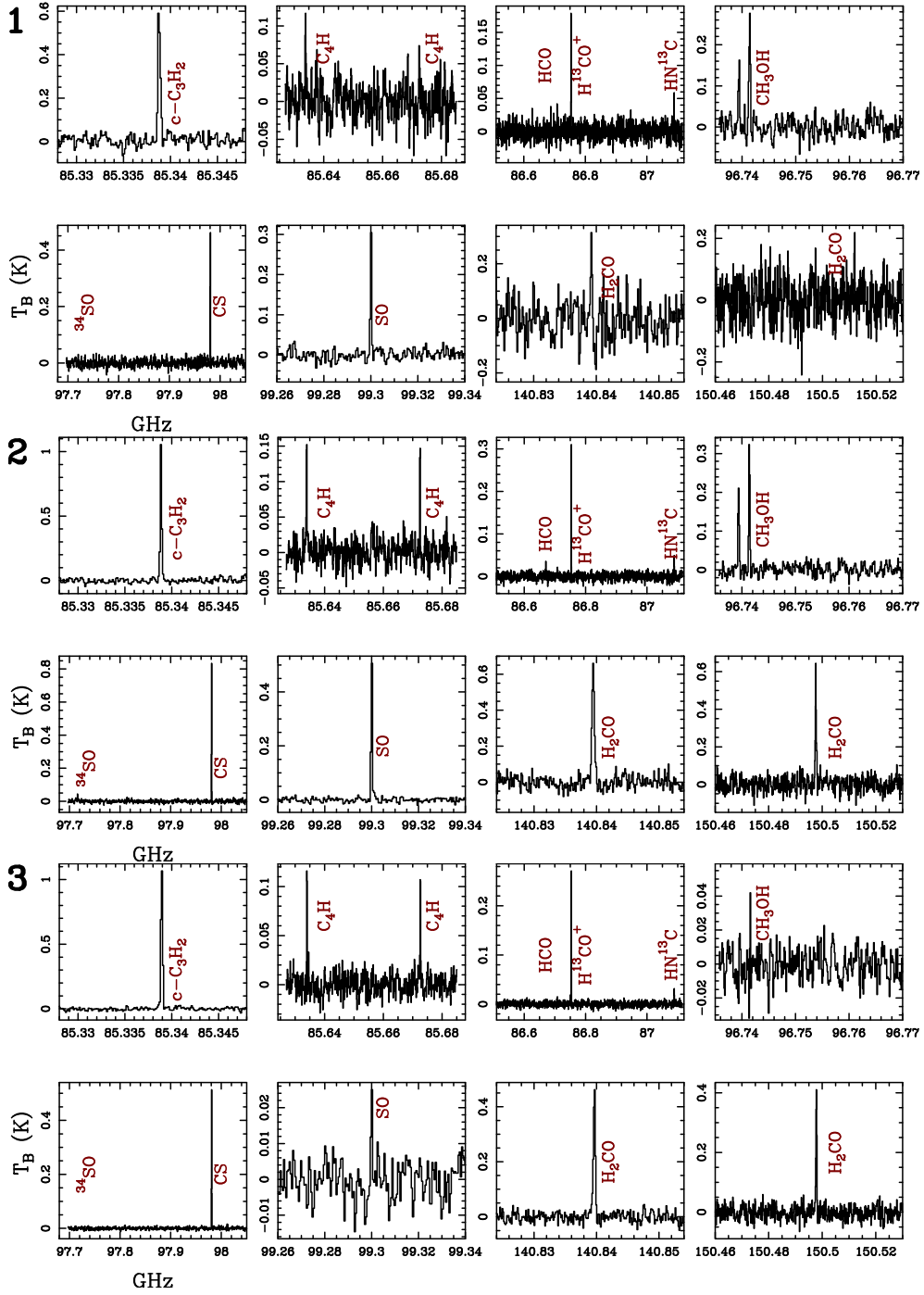


Fig. B.1. Spectra extracted from the $c\text{-C}_3\text{H}_2$ region 1, 2, and 3, from top to bottom, in brightness temperature (T_B) units. On the x-axis we show the rest frequency.

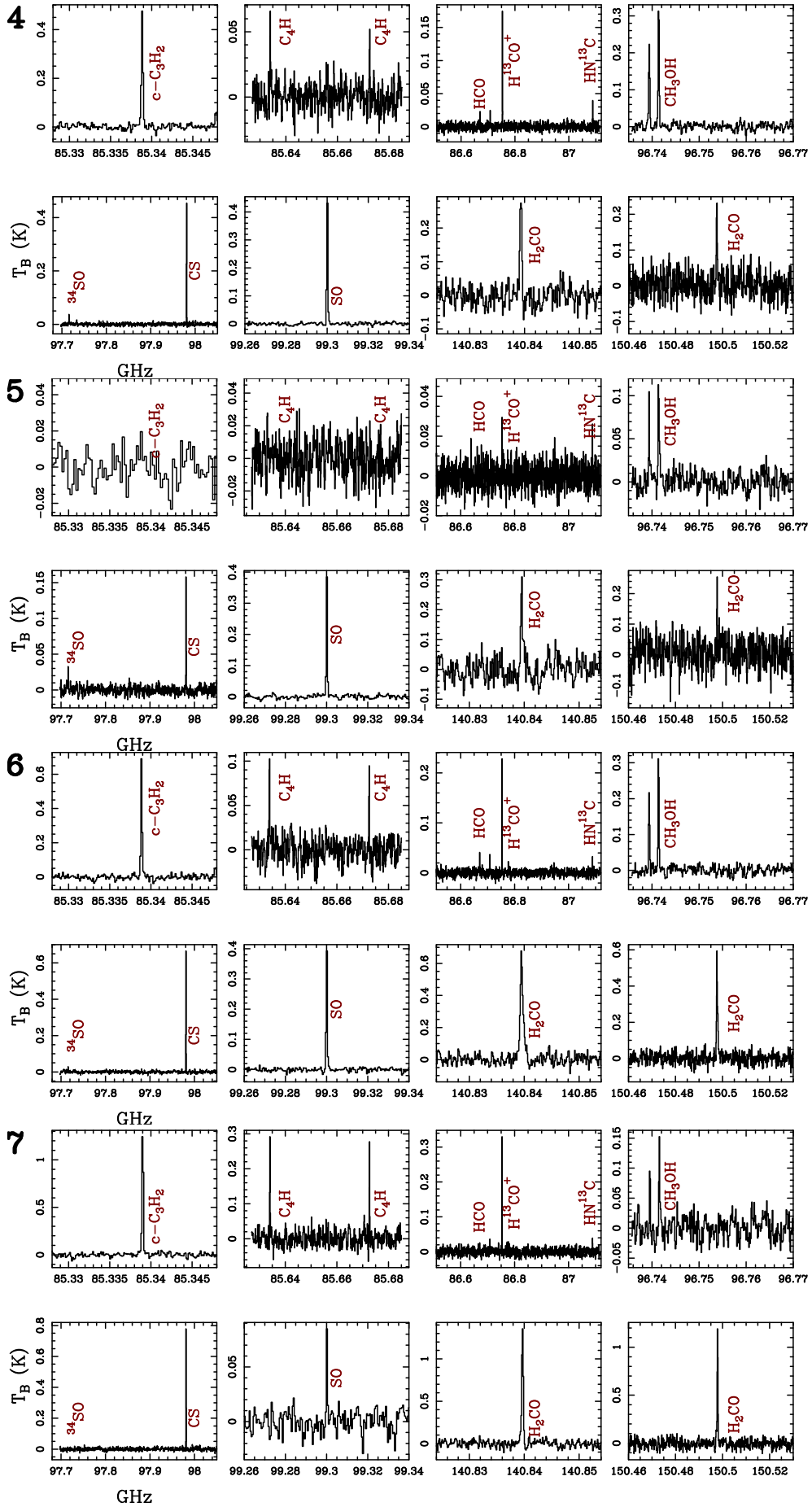


Fig. B.2. Same as Fig. B.1 for the regions 4, 5, 6, and 7, from top to bottom.

Appendix C: Fit results

Fit results obtained with MADCUBA and CLASS towards the lines detected in the seven molecular emitting regions identified in Fig. 4.

Table C.1. Fit results of the molecular lines identified in region 1.

molecule	N_{tot} (10^{12}cm^{-2})	T_{ex} (K)	v_{LSR} (km s^{-1})	FWHM (km s^{-1})
MADCUBA ^a				
C ₄ H	5.1(0.3)	6.4	-17.02(0.09)	0.79(0.05)
<i>c</i> -C ₃ H ₂	6.5(0.2)	6.4	-17.70(0.01)	0.75(0.02)
CH ₃ OH	0.9(0.3)	6.4(0.9)	-18.1(0.2)	0.7
HCS ⁺	0.04(0.01)	6.4	-17.1(0.08)	0.7
H ₂ CO	5(1)	6.4	-17.1	0.7
CLASS ^c				
molecule	N_{tot} (10^{12}cm^{-2})	$\int T_{\text{B}}\text{d}v$ (K)	v_{LSR} (km s^{-1})	FWHM (km s^{-1})
HCO ^c	≤ 1.9	–	–	–
H ¹³ CO ⁺	8.7(1.1)	0.59(0.02)	-17.82(0.05)	1.89(0.09)
HN ¹³ C	2.8(0.7)	0.09(0.01)	-17.4(0.2)	2.3(0.6)
SO	6.3(1.9)	0.06(0.01)	-17.9(0.1)	– ^d
CS	68(7)	1.18(0.01)	-17.28(0.01)	2.16(0.02)

Notes. Line parameters without uncertainties (quoted in brackets) were fixed in the fit. The error on N_{tot} contains the calibration error of $\sim 10\%$ when derived with CLASS, while does not when derived with MADCUBA. Hence, in this case the total uncertainty is given by the quadrature sum of the quoted error and of a 10% calibration error. ^(a) Parameters obtained fitting the lines with MADCUBA; ^(b) Parameters obtained fitting the lines with CLASS; ^(c) Parameters obtained fitting with a Gaussian profile the hyperfine component $F = 1 - 0$, detected in almost all regions except regions 1 and 5; ^(d) Parameter not constrained because the uncertainty provided by the fit is higher than the output value.

Table C.2. Same as Table C.1 for region 2.

MADCUBA ^a				
molecule	N_{tot} (10^{12}cm^{-2})	T_{ex} (K)	v_{LSR} (km s^{-1})	FWHM (km s^{-1})
C ₄ H	7.6(0.6)	8.3	-17.14(0.02)	0.76(0.08)
<i>c</i> -C ₃ H ₂	5.1(0.2)	8.3	-17.39(0.01)	0.62(0.02)
CH ₃ OH	13.5(3)	8.3(1.3)	-17.56(0.03)	0.74(0.06)
HCS ⁺	0.5(0.1)	8.3	-17.4(0.2)	1.70(0.5)
H ₂ CO	8(1)	8.3	-17.5	1.0
CLASS ^b				
molecule	N_{tot} (10^{12}cm^{-2})	$\int T_{\text{B}}\text{d}v$ (K)	v_{LSR} (km s^{-1})	FWHM (km s^{-1})
HCO ^c	6(5)	0.15(0.1)	-17(2)	– ^d
H ¹³ CO ⁺	8.6(1.2)	0.62(0.03)	-17.38(0.06)	1.86(0.08)
HN ¹³ C	3.7(1.0)	0.13(0.02)	-17.5(0.1)	– ^d
SO	91(10)	1.06(0.02)	-18.07(0.03)	1.79(0.05)
CS	84(9)	1.75(0.02)	-17.00(0.04)	1.81(0.03)

Table C.3. Same as Table C.1 for region 3.

MADCUBA ^a				
molecule	N_{tot} (10^{12}cm^{-2})	T_{ex} (K)	v_{LSR} (km s^{-1})	FWHM (km s^{-1})
C ₄ H	10(2)	6.4	-17.02(0.09)	1.15(0.2)
<i>c</i> -C ₃ H ₂	4.6(0.4)	6.4	-17.18(0.04)	1.1(0.1)
CH ₃ OH	12(5)	6.4(1.3)	-17.71(0.04)	0.95(0.09)
HCS ⁺	0.5(0.08)	6.4	-17.45(0.08)	1.1(0.2)
H ₂ CO	5.0(1.0)	6.4	-17.5	1.0
CLASS ^b				
molecule	N_{tot} (10^{12}cm^{-2})	$\int T_{\text{B}}\text{d}v$ (K)	v_{LSR} (km s^{-1})	FWHM (km s^{-1})
HCO ^c	8(4)	0.17(0.06)	-17.0(0.7)	3.8(1.6)
H ¹³ CO ⁺	5.7(1.0)	0.39(0.03)	-17.2(0.1)	1.8(0.2)
HN ¹³ C	3.8(1.4)	0.12(0.03)	-17.9(0.5)	2.0(0.5)
SO	69(10)	0.61(0.03)	-18.14(0.08)	1.8(0.1)
CS	65(8)	1.13(0.03)	-16.79(0.04)	1.8(0.2)

Table C.4. Same as Table C.1 for region 4.

MADCUBA ^a				
molecule	N_{tot} (10^{12}cm^{-2})	T_{ex} (K)	v_{LSR} (km s^{-1})	FWHM (km s^{-1})
C ₄ H	2.9(0.4)	8.4	-17.25(0.05)	0.86(0.13)
<i>c</i> -C ₃ H ₂	2.6(0.1)	8.4	-17.38(0.01)	0.76(0.03)
CH ₃ OH	16(3)	8.4(1.2)	-17.59(0.03)	0.83(0.06)
HCS ⁺	0.4(0.05)	8.4	-17.2	0.8
H ₂ CO	2.0(0.3)	8.4	-17.1	0.7
CLASS ^b				
molecule	N_{tot} (10^{12}cm^{-2})	$\int T_{\text{B}}\text{d}v$ (K)	v_{LSR} (km s^{-1})	FWHM (km s^{-1})
HCO ^c	2.7(1.8)	0.07(0.004)	-16.2(0.8)	2.5(1.3)
H ¹³ CO ⁺	5.0(0.7)	0.36(0.01)	-17.54(0.05)	1.92(0.06)
HN ¹³ C	2.6(0.6)	0.09(0.01)	-17.4(0.1)	1.7(1.3)
SO	75(9)	0.88(0.01)	-18.17(0.02)	1.83(0.03)
CS	50(6)	1.06(0.01)	-16.86(0.02)	1.85(0.05)

Table C.5. Same as Table C.1 for region 5.

MADCUBA ^a				
molecule	N_{tot} (10^{12}cm^{-2})	T_{ex} (K)	v_{LSR} (km s^{-1})	FWHM (km s^{-1})
C ₄ H	≤ 3.2	15	–	–
<i>c</i> -C ₃ H ₂	– ^e	–	–	–
HCS ⁺	≤ 0.09	15	–	–
H ₂ CO	1.7(0.3)	15	–17.64(0.07)	0.9(0.2)
CLASS ^b				
molecule	N_{tot} (10^{12}cm^{-2})	$\int T_{\text{B}}\text{d}v$ (K)	v_{LSR} (km s^{-1})	FWHM (km s^{-1})
CH ₃ OH	10(1)	15	–17.66(0.04) ^f	0.9(0.1) ^f
HCO ^c	≤ 1.5	–	–	–
H ¹³ CO ⁺	0.8(0.3)	0.05(0.01)	–17.6(0.5)	1.7(1.5)
HN ¹³ C	1.8(0.6)	0.06(0.01)	–17.4(0.2)	– ^d
SO	48(6)	0.72(0.01)	–18.33(0.03)	1.76(0.03)
CS	14(2)	0.35(0.01)	–17.55(0.05)	2.0(0.1)

Notes. ^(e) Fit not performed because the line shows self-absorption at line centre; ^(f) Derived from the line at 96.7414 GHz.

Table C.6. Same as Table C.1 for region 6.

MADCUBA ^a				
molecule	N_{tot} (10^{12}cm^{-2})	T_{ex} (K)	v_{LSR} (km s^{-1})	FWHM (km s^{-1})
C ₄ H	10(0.6)	9	–17.72(0.02)	0.69(0.05)
<i>c</i> -C ₃ H ₂	7.6(0.2)	9	–17.91(0.01)	0.68(0.02)
CH ₃ OH	6(2)	9.4(2.3)	–18.12(0.04)	0.62(0.08)
HCS ⁺	0.23	9	–17.3	0.9
H ₂ CO	10.0(1.1)	9	–17.8	0.9
CLASS ^b				
molecule	N_{tot} (10^{12}cm^{-2})	$\int T_{\text{B}}\text{d}v$ (K)	v_{LSR} (km s^{-1})	FWHM (km s^{-1})
HCO ^c	4(3)	0.09(0.06)	–16.9(0.7)	– ^d
H ¹³ CO ⁺	11.4(1.5)	0.82(0.02)	–17.07(0.02)	1.7(0.6)
HN ¹³ C	3.5(1.1)	0.12(0.03)	–17.3(0.3)	2.7(0.7)
SO	12(3)	0.16(0.02)	–18.5(0.2)	1.7(0.2)
CS	73(8)	1.63(0.02)	–17.65(0.02)	1.79(0.04)

Table C.7. Same as Table C.1 for region 7.

MADCUBA ^a				
molecule	N_{tot} (10^{12}cm^{-2})	T_{ex} (K)	v_{LSR} (km s^{-1})	FWHM (km s^{-1})
C ₄ H	4.4(0.4)	8.4	-17.18(0.03)	0.73(0.09)
<i>c</i> -C ₃ H ₂	3.2(0.1)	8.4	-17.40(0.01)	0.60(0.02)
CH ₃ OH	14(3)	8.4(1.3)	-17.59(0.03)	0.73(0.06)
HCS ⁺	0.3(0.06)	8.4	-17.3(0.1)	0.9(0.2)
H ₂ CO	5(1)	8.4	-17.5	0.8
CLASS ^b				
molecule	N_{tot} (10^{12}cm^{-2})	$\int T_{\text{B}}\text{d}v$ (K)	v_{LSR} (km s^{-1})	FWHM (km s^{-1})
HCO ^c	5(3)	0.12(0.06)	-16.0(0.8)	2.9(1.9)
H ¹³ CO ⁺	7.0(1.0)	0.50(0.02)	-17.48(0.06)	2.07(0.08)
HN ¹³ C	2.3(0.7)	0.08(0.01)	-17.4(0.1)	- ^d
SO	70(8)	0.82(0.01)	-18.16(0.02)	1.89(0.04)
CS	69(8)	1.45(0.02)	-17.14(0.01)	2.00(0.02)